Figure Rotation of Dark Halos in Cold Dark Matter Simulations

by
Sarah Bryan

Submitted in fulfilment of the academic requirements
for the degree of Master of Science in the
School of Physics,
University of KwaZulu-Natal

Pietermaritzburg
December, 2005

Declaration

I declare that this work is a result of my own research, except where specifically indicated to the contrary, and has not been submitted for any other degree or examination to any other University.

Signed: _____   Date: _21 · 04 · 06_____

Supervisor ·

Acknowledgements

I wish to express my sincerest gratitude to all of the people that have been involved in this project, for the support and encouragement they have provided in the preparation of this work.

In particular I would like to thank my supervisor Dr. Cress for her support and guidance throughout this project, her constant enthusiasm has kept me motivated and contributed to both my academic and personal growth.

My heartfelt thanks to my family, for their patience and understanding, for providing a foundation without which this work would not have been possible. Thanks also to Dion whose love, encouragement and inspiration has proved invaluable.

Abstract

We have simulated structure formation on cosmological-scales using N-body simulations run on the University of KwaZulu-Natal's cluster of computers and have used these simulations to investigate aspects of galaxy evolution. In particular, we focus on the rotation of dark matter halos identified in Cold Dark Matter (CDM) simulations. These halos are typical of those thought to surround galaxies. Understanding their morphology and kinematics will help with the interpretation of observations and will constrain models of galaxy formation and evolution.

We have determined the mass function of our simulated halos and shown that this agrees well with other simulations and theoretical predictions of this function. We have also explored the evolution of the mass function with redshift, which clearly shows hierarchical structure formation. In considering the angular momentum of our sample of halos, we have found the spin distribution to be well fit by a log normal distribution (best fit values of $\lambda_0' = 0.04$ and $\sigma = 0.6$). After removing all halos that have either recently undergone major mergers or contain a significant amount of substructure from our sample, 75% of the remaining halos were found to undergo coherent rotation over periods of three gigayears. The pattern speeds were found to follow a log normal distribution, with an average value of $0.13h$ radians per gigayear. The most rapidly rotating halo detected was found to have a pattern speed of $0.41h$ radians per gigayear. Many halos showed alignment between their rotation and minor axes. We found no correlation between halo properties, such as total mass, and the pattern speed. While the speeds observed were not sufficient to cause spiral structure, the rotation could be relevant for understanding other observations of galaxies.

Contents

List of Tables

List of Figures

Chapter 1

Introduction

Over the past 30 years our understanding of the cosmological setting, within which galaxies form and evolve, has grown dramatically thanks to a huge increase in the amount of extragalactic data available. We observe galaxies, clusters of galaxies, superclusters, filaments: an abundance of structure. On the other hand observations of the Cosmic Microwave Background (CMB) provide evidence that the universe was initially very smooth. Understanding how galaxies form and evolve from this initial state is an active area of research.

It is often assumed that the density fluctuations in the universe result from quantum fluctuations which are greatly amplified during an inflationary phase very early in the universe. The resulting overdensities become more and more overdense with time, collapsing under the influence of gravity. Eventually these overdense regions are thought to become sites for the formation of structures such as galaxies, while the underdense regions are thought to become voids. A first step in understanding the formation of such structure comes from studying the linear theory of density perturbations. We can explain structure formation using simple hydrodynamical results in the linear regime (where fluctuations in density are small compared with the average density) however, complications arise in the non-linear regime where these results no longer apply. In order to study this complicated era, simulations become an essential tool.

N-body simulations model the universe as a system of a finite number of particles. Given the initial position and velocity of each particle, one can follow the evolution of the system numerically by repeatedly applying Newton's equations of motion. In order to create a reliable model, large particle numbers and small time steps are required. The rapid advances in both computing power and numerical techniques have made these large simulations feasible.

Observations of the CMB, large-scale structure and supernovae have led to the Lambda Cold Dark Matter (ΛCDM) model being adopted as the standard cosmological model [Spergel et al., 2003]. According to this model the present universe is made up of radiation (negligible contribution), baryonic matter (4%), cold dark matter (CDM $\sim$ 26%) and dark energy ($\Lambda \sim$ 70%). The universe is modelled as homogenous, isotropic and flat ($\Omega_{matter} + \Omega_\Lambda = 1$, where Ω is the ratio of density to critical density). The model also assumes a nearly scale invariant spectrum of primordial fluctuations ($n_s \sim$ 1). These properties (flatness and scale-invariance) are predictions of cosmic inflation. Most of the present day universe is made up of dark energy, which in the ΛCDM model takes the form of a cosmological constant. This energy has a strong negative pressure and is responsible for the accelerating expansion of the universe. Most of the remaining mass of the universe is made up of cold dark matter particles, these particles are non-baryonic and collisionless. Cold dark matter particles are termed 'cold' because they are non-relativistic at the time of decoupling, moving at speeds well below that of the speed of light and hence forming cold gases. The ΛCDM model successfully explains the expansion of the universe, the existence of the Cosmic Microwave Background, large-scale homogeneity and isotropy and the light element abundances. The evidence supporting this model is extremely strong. Table 1.1 lists the current values for some of the parameters of this model. The values are taken from the data obtained by the Sloan Digital Sky Survey combined with data from the Wilkinson Microwave Anisotropy Probe (WMAP) [Tegmark et al., 2004].

In the standard model galaxies form and evolve within underlying dark matter struc-

Parameter	Parameter Value	Description
H_0	$69.5^{+3.9}_{-3.1}$ km s^{-1} Mpc^{-1}	Hubble parameter
ρ_0	$0.91^{+0.10}_{-0.08} \times 10^{-26}$ kg m^{-3}	Critical density
Ω_m	$0.301^{+0.045}_{-0.042}$	Total matter density (CDM + baryons)
Ω_Λ	$0.699^{+0.042}_{-0.045}$	Dark energy density
Ω_b	$0.0480^{+0.072}_{-0.0067}$	Baryon density
σ_8	$0.917^{+0.090}_{-0.072}$	Galaxy fluctuation amplitude
n_s	$0.977^{+0.039}_{-0.025}$	Scalar spectral index

Table 1.1: Standard ΛCDM Parameters

Cosmological parameters from SDSS and WMAP [Tegmark et al., 2004].

tures, and the morphology and kinematics of the dark matter clearly affects the development of the galaxies. Identifying and observing the effects of the motion of dark matter provides another test of the cold dark matter model.

The dark matter surrounding a galaxy (extending well beyond the optically observed region) is known as the 'halo'. We focus our attention on the possible tumbling motion (figure rotation) of the dark matter halos. Figure rotation refers to the change in orientation of the entire halo, ignoring the motion of the constituent particles. Initially calculations of stellar orbits in galaxies ignored the dark matter halo completely. Then, as observational evidence for dark matter halos increased [Gunn, 1980], these calculations involved modelling the halos as stationary spherical objects. Further investigation into dark matter halos indicated that many halos were in fact triaxial [Dubinski and Carlberg, 1991; Warren et al., 1992] and not spherical as had been assumed. This is now taken into consideration, however, orbits are still modelled within stationary dark matter halos, these calculations fail to take into account the effect of figure rotation.

Bekki and Freeman [2002] suggest that figure rotation of the dark halo would play an important role in the formation and evolution of the embedded galaxies. In par-

ticular, they suggest that figure rotation may influence the formation of stellar bars as well as spiral arms and warps. They also suggest that figure rotation could trigger star-bursts in galaxies, even at high redshifts. Since orbits passing near the centre of galaxies are affected, figure rotation could also have consequences for black hole growth in galaxies [de Zeeuw and Franx, 1991] and the so-called 'cusp/core problem' [de Blok et al., 2001]. Observations of such effects could be used to constrain current galaxy formation theories.

Initial work on the subject of figure rotation was done by Dubinski in 1992. In a paper discussing the effects of cosmological tidal shear [Dubinski, 1992], Dubinski considered the kinematics and structure of dark matter halos produced by N-body simulations. This study included 14 dark matter halos evolved using a modified tree code incorporating the effect of a tidal field, as described by Dubinski and Carlberg [1991], as well as a control sample of 14 halos simulated with vacuum boundary conditions. Two larger simulations were run to provide higher resolution results for both sets of conditions. Dubinski found that the simulated halos evolved with tidal effects experienced a noticeable rotation. The halos were found to have tumbling speeds ranging from 0.1 to 1.6 radians per gigayear. (These units are essentially equivalent to km s^{-1} kpc^{-1}). Dubinski concluded that the effects of this tumbling would not have a significant impact on the dynamics of the galaxies since the tumbling period was so much shorter (of the order $10 - 100$ times) than the orbital period of the halo. However, he noted the significant effect tidal shear played in determining the shape of dark matter halos. The small sample size and somewhat artificial implementation of the tidal field, meant further studies in this area were necessary.

Pfitzner [1999], while working on his PhD thesis, noticed that a significant number of triaxial halos produced in cold dark matter simulations tended to rotate steadily around their minor axes. One such halo was extracted from the simulation at late times and was allowed to evolve in isolation over a five gigayear period. During this time the halo was found to rotate as a solid body with constant pattern speed (tum-

bling speed) of about 1.1 radians per gigayear.

In 1999, Bureau et al. discussed possible causes for the spiral pattern observed in the isolated blue dwarf galaxy NGC 2915. They considered it unlikely that gravitational interaction was responsible for the pattern as the galaxy was isolated, and that the surface density in the disk was too low for swing amplification to cause the spiral pattern. They proposed that slow figure rotation of a surrounding triaxial dark halo may be responsible for creating the spiral structure seen in NGC 2915 and encouraged further studies of gas disks contained within the potentials of rotating triaxial dark halos.

Bekki and Freeman [2002] continued this work, using numerical simulations. In this study they showed that a 'slowly' rotating triaxial dark halo could cause large spiral arms in an extended gas disk, and that the resulting structure is strongly dependent on the pattern speed of the halo. This work emphasised the importance of the dynamics of dark halos in galaxy formation and evolution.

Masset and Bureau [2003] further explored the effects of a rotating triaxial dark halo proposed by Bureau et al. [1999], using hydrodynamical simulations and concluded that, while a rotating triaxial halo could be responsible for causing spiral structure, the required pattern speed was prohibitively large - between 5.5 and 6.5 radians per gigayear.

The most recent work done regarding the figure rotation of dark matter halos was conducted by Bailin and Steinmetz in 2004. They selected 317 undisturbed halos from a large, high resolution Λ cold dark matter N-body simulation. They compared the orientation of the major axis determined from the central sphere (radius of $0.6 \times$ virial radius) of each of these halos over five time intervals (a total period of just over one gigayear). From the sample of 317 halos they found that 278 (88 %) of their halos did indeed rotate smoothly, with pattern speeds of around $0.15h$ (where $H_0 = 100\ h$ km

s^{-1} Mpc^{-1}) radians per gigayear. They noted that the pattern speeds observed in the inner regions of the undisturbed halos in their sample were not sufficient to cause the spiral patterns as discussed by Bureau et al. [1999].

In this project, we have simulated the evolution of structure in a 50 h^{-1} Mpc cubed region of space, using initial conditions consistent with Cosmic Microwave Background observations. We have used GADGET, an N-body code to evolve the positions and velocities of 256^3 (16 777 216) collisionless particles. These particles fall together under gravity, forming dark matter halos. Halos are identified from the simulation by using a simple friends-of-friends algorithm. We explore the figure rotation of the simulated dark matter halos, which are typical of the halos we expect to surround galaxies, over a period of one and three gigayears. To do this we have identified halos from simulation outputs at a redshift of zero, then traced them back through time. We did not limit ourselves to a central sphere, but considered the halo in its entirety. By following the motion of the principal axis of the whole halo over several time steps, we are able to measure the pattern speed of the figure rotation of that halo.

In chapter 2, we begin with a discussion of some of the techniques used in N-body simulations. We also include a description of GADGET, the details of our simulation and a discussion of the advantages of parallelisation. Then, in chapter 3, we describe the process used in analysing the output of a simulation, including how we identify and follow halos through time, the calculation of the inertia tensor and principal axis of a halo and the determination of a halo's pattern speed. Chapter 4 gives the results of our analysis. We discuss the results and draw conclusions in chapter 5. Appendix A describes the visualisation techniques used in this project. Appendix B presents linear structure formation theory and Appendix C provides a discussion on the theory of rigid body rotation. Appendix D provides plots of all fits used to calculate the pattern speeds of our simulated halos.

Chapter 2

Methodology I: Simulations

The non-linear nature of the mass distribution on small scales and the complexity of hydrodynamic processes mean simple well known fluid dynamic equations (see Appendix B) are no longer applicable when trying to describe the evolution of density fluctuations in the universe. Supercomputer simulations are thus essential for the construction of realistic models of galaxy formation.

2.1 N-body Codes

An N-body problem can be defined as the evolution of a system of N particles over time. Each particle will experience a force due to its interaction with the surrounding particles. At each time step, the force experienced by each particle needs to be calculated, using the attributes of the other particles acting upon it.

2.1.1 Direct Method

Initial work with simulations employed a technique known as the Particle - Particle or Direct Method. This method is the simplest of the N-body codes. The force exerted on a particle is found by summing up the forces exerted on that particle by every other particle in the simulation. While accurate, this method is computationally intensive in cosmological simulations where interactions are dominated by gravity. Forces are

found using the 'modified' version of Newton's Law of Gravitation

$$F = \nabla \sum_{i \neq j} \frac{G\, m_i\, m_j}{(x_{ij}^2 + \epsilon^2)^{\frac{1}{2}}} .$$

(2.1)

In this equation the parameter ϵ is introduced to implement force softening. This is required to avoid numerical instability and prevent two-body collisions from driving the simulation. If the denominator in equation 2.1 is allowed to tend to zero the force will approach infinity. An infinite force will cause an infinite acceleration, and an infinitely small time step would be required to follow the particle. A second reason for introducing the force softening parameter is a physical one: particles with masses of the order 10^7 solar masses are so large that the notion of a very close encounter between them is unphysical. The force softening parameter ϵ, is chosen to be as small as possible to achieve the highest possible resolution (see section 2.5.3). While the direct method allows for a very accurate force calculation, it is obviously a computationally intensive technique (of the order N^2) and it rapidly becomes infeasible as particle numbers increase.

2.1.2 Mesh Codes

While the direct method is accurate, its usefulness is limited for large particle numbers. To overcome this limitation, mesh codes, which make use of Fourier techniques, were developed. These mesh codes are particularly well suited to modelling distributions which are close to homogenous.

Particle Mesh

The Particle-Mesh approach uses a grid implementation in which each particle is associated with its nearest grid point. Using the particle positions, the density ρ at each grid point is calculated. Poisson's equation $\left(\nabla^2 \phi = -\rho\,(x)\right)$ is then solved, using Fast Fourier methods, to determine the potential at each grid point. The potential is differentiated to find the force for each grid point, this is then interpolated to establish the force on each particle. Using this approach greatly reduces the computational cost of

a simulation from an N^2 operation in the Direct Method, to an N log N order computation. However, the resolution of the simulation is dependent on the chosen grid size.

Particle[3] Mesh

The Particle Particle Particle Mesh or P[3]M algorithm was developed by Efstathiou and Eastwood [Efstathiou et al., 1985; Efstathiou and Eastwood, 1981]. It uses a combination of the methods discussed above to create an efficient, high resolution approach. The gravitational acceleration calculation is divided into two components. Short range components (forces attributed to particles within a specified radius r_s) are found using the Direct Method, while long range components are determined using the Particle Mesh approach. The radius which separates these components depends on the system size, and is generally set to be about 0.05 times the length of the simulated cube.

Essentially

$$\mathbf{F}_i = \mathbf{F}_i(SR) + \mathbf{F}_i(LR) \tag{2.2}$$

where $\mathbf{F}_i$ is calculated using
$\mathbf{F}_i$ (SR) = Particle Particle for small distances ($r < r_s$)
$\mathbf{F}_i$ (LR) = Particle Mesh for large distances ($r > r_s$)

This method combines the advantages of both the Direct Method and the Particle Mesh approach, allowing it to manage large particle number simulations with sufficient accuracy.

2.1.3 Tree Algorithms

While mesh codes are well suited to homogeneous distributions of particles, problems often involve a high level of clustering. In order to improve performance one can employ

a tree algorithm. The tree algorithm is particularly suited to clustered distributions and can readily adapt to any geometry. The tree algorithm involves grouping the particles of a simulation in a hierarchial manner. The gravitational field at any point in the simulation is then found by summing the multipole expansions of these groups. Grouping of the particles can be achieved by various means. This method is an order $N \log N$ scheme. We discuss the implementation of the tree algorithm further in section 2.3.

2.2 Parallel Computing

Even with the efficient algorithms discussed earlier in this chapter, large particle number simulations are limited by the hardware available today. The large amount of memory required to accurately simulate most problems is often larger than the memory available on a single computer. To improve the situation, parallelised systems are used. By combining the computational power of several machines we are able to simulate far larger particle numbers than would be possible on a single processor.

When GADGET is run on a serial machine the amount of memory allocated for particle storage is proportional to the number of particles contained within the simulation. For a simulation each particle requires 225 bytes of memory. This means that 128^3 particles would require 0.5 Gbytes of memory. Going beyond this pushes the limits of an ordinary workstation. Parallel computation provides the user with more memory by utilising the combined memory of a cluster of machines, however there is the added cost of communication between processors. For a parallel run, memory is required for particle storage as well as for communication buffers.

Locally we have a cluster of fourteen processors, each of which has two gigabytes of memory. However, the algorithm used by GADGET requires the number of processors used to be a power of two, and we are therefore limited to a maximum of eight processors for our simulations. For this reason we have chosen to use 256^3 particle

simulation for this project, which fits comfortably into the memory available on the cluster.

To explore the effects of parallelisation, we have run a small 32^3 simulation on a serial machine as well as on two, four and eight processors of the cluster. The simulation took ten minutes to complete when run on a single machine. The same simulation was completed in 1.5 minutes on 8 processors. Figure 2.1 shows the computation time required versus the number of processes. As one would expect, as the number of processors is increased the computation time decreases as the workload is split among the processors. The cost of communication between processors is noticeable. Figure 2.2 shows the amount of time required for communication between processors, this increases with the number of processors used, as expected.
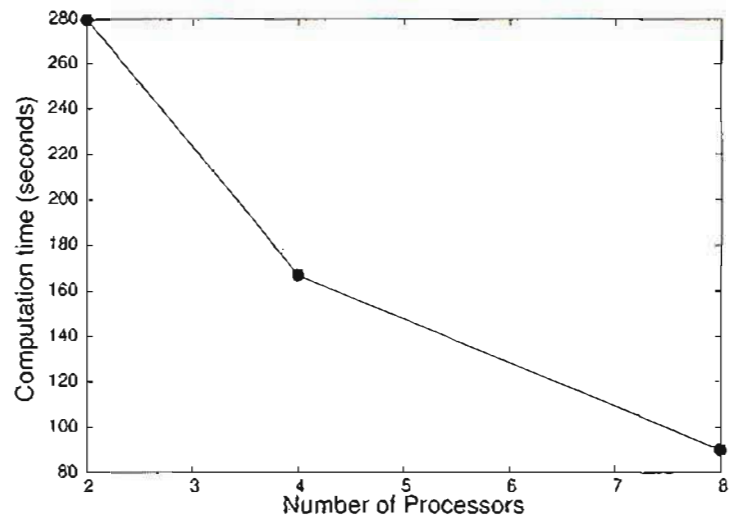
Figure 2.1: Computation Time versus Number of Processors
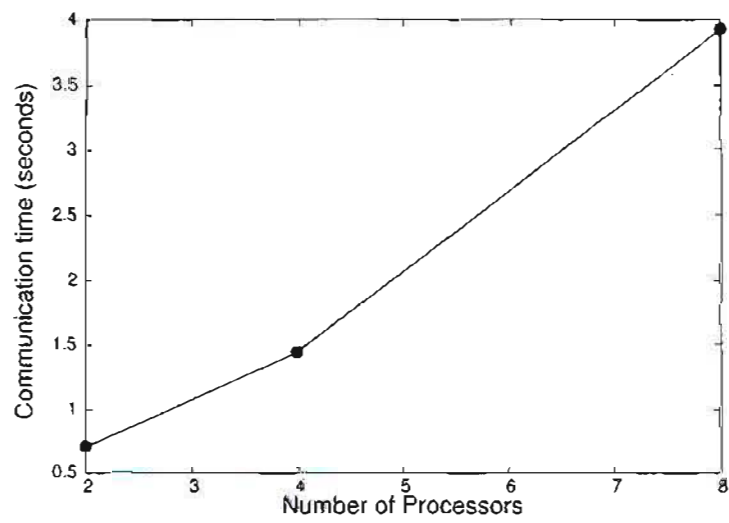
Figure 2.2: Communication Time versus Number of Processors

12

2.3   GADGET

GADGET (GAlaxies with Dark matter and Gas intEracT) is the publicly available N-body code that was used throughout this project. For a full description of the code we refer the reader to "GADGET: a code for collisionless and gasdynamical cosmological simulations" [Springel et al., 2001]. GADGET is a highly adaptable N-body code which can be used for a variety of problems.

Dark matter is modelled as a self-gravitating collisionless fluid and will therefore evolve according to the collisionless Boltzmann equation (CBE)

$$\frac{df}{dt} \cong \frac{\partial f}{\partial t} + \mathbf{v}\frac{\partial f}{\partial \mathbf{x}} - \frac{\partial \phi}{\partial \mathbf{x}}\frac{\partial f}{\partial \mathbf{v}} = 0 \tag{2.3}$$

where the potential is given by the solution of Poisson's equation

$$\nabla^2 \phi(\mathbf{x},t) = 4\pi G \int f(\mathbf{x},\mathbf{v},t)\, d\mathbf{v} \tag{2.4}$$

and $f(\mathbf{x},\mathbf{v},t)$ is the distribution function describing the mass density in single particle phase space. Solving these coupled equations using finite-difference methods is very difficult and often a numerical approach is adopted. GADGET employs a Monte Carlo technique in which the phase fluid is represented by N particles. The N-body realization is then evolved according to Newton's equations of motion

$$\frac{d\mathbf{r}_\alpha}{dt} = \mathbf{v}_\alpha \qquad\qquad \frac{d\mathbf{v}_\alpha}{dt} = -\nabla\phi\,|_{r=r_\alpha}. \tag{2.5}$$

2.3.1   Multipole Expansion of the Gravitational Force

The potential at r due to a distant group of particles with mass m_α and co-ordinates $\mathbf{x}_\alpha$ can be expressed as

13

$$\Phi(\mathbf{r}) = -G \sum_\alpha m_\alpha \, g\left(|\mathbf{x}_\alpha - \mathbf{r}|\right) \tag{2.6}$$

where $g(r)$ is a function used to describe the softened force law. For Newtonian gravity $g(r) = \frac{1}{r}$. GADGET uses a spline softened force law which is exactly Newtonian for r greater than the force softening distance (ϵ) and which converges rapidly to the Newtonian force for r less than ϵ.

To obtain a multipole expansion of the potential at r, let s be the centre of mass coordinate of the distant group of particles, M the total mass of the particles and define $\mathbf{y} \equiv \mathbf{r} - \mathbf{s}$. If we assume that $|\mathbf{x}_\alpha - \mathbf{s}| \ll |\mathbf{y}|$ equation 2.6 can be expanded to obtain a multipole series, the quadrupole approximation of which is given by

$$\Phi(\mathbf{r}) = -G\left\{ M\, g(y) + \frac{1}{2}\, \mathbf{y}^T \left[\frac{g''(y)}{y^2}\, \mathbf{Q} + \frac{g'(y)}{y^3}(\mathbf{P} - \mathbf{Q}) \right] \mathbf{y} \right\} \tag{2.7}$$

where the tensors $\mathbf{Q}$ and $\mathbf{P}$ are defined as follows

$$\mathbf{Q} = \sum_\alpha m_\alpha \, \mathbf{x}_\alpha \, x_\alpha^T - M\, \mathbf{s}\, \mathbf{s}^T \tag{2.8}$$

$$\mathbf{P} = \mathbf{I} \left[\sum_\alpha m_\alpha \mathbf{x}_\alpha^2 - M\mathbf{s}^2 \right]. \tag{2.9}$$

The quadrupole approximation of the softened gravitational field $(-\nabla\Phi)$ is then

$$\mathbf{f}(\mathbf{r}) = G\left\{ M\, g_1(y)\, \mathbf{y} + g_2(y)\, \mathbf{Q}\, \mathbf{y} + \frac{1}{2}\, g_3(y)\, (\mathbf{y}^T \mathbf{Q}\, \mathbf{y})\mathbf{y} + \frac{1}{2}\, g_4(y)\, \mathbf{P}\, \mathbf{y} \right\} \tag{2.10}$$

14

where

$$g_1(y) = \frac{g'(y)}{y}$$
$$g_2(y) = \frac{g''(y)}{y^2} - \frac{g'(y)}{y^3}$$
$$g_3(y) = \frac{g_2'(y)}{y}$$
$$g_4(y) = \frac{g_1'(y)}{y} \ .$$

(2.11)

2.3.2 Particle Grouping

GADGET employs a tree algorithm. In order to group the particles, GADGET uses a Barnes and Hut approach (illustrated in figure 2.3). This approach partitions a cube of space into eight cubes, by halving the length of each side of the original (parent) cube. The eight new cubes are known as sibling cubes or children of the parent cube. This partitioning is continued until the leaf nodes (nodes that have no children) contain no more than one particle each. Each cube which is not a leaf node has a record of both the monopole and quadrupole moments of all of the particles that are contained within the cube. In order to calculate a force one simply needs to traverse the tree, adding the force contributions from each cube (node). In determining whether the multipole expansion of the node may be used or whether the walk along the tree must be continued a 'cell opening criteria' is established, this depends on the required accuracy of the simulation.

2.3.3 Time Step

GADGET uses an adaptation of the leap frog approach in determining the time step. The leap frog method involves predicting the position of a particle in the middle of a time step, then finding its acceleration based on its position. The velocity of a particle for the next time step is then determined using the acceleration at the half-timestep interval. This velocity is then used to calculate the particles position at the next time interval. GADGET allows each particle to evolve at its own rate, allowing flexibility.
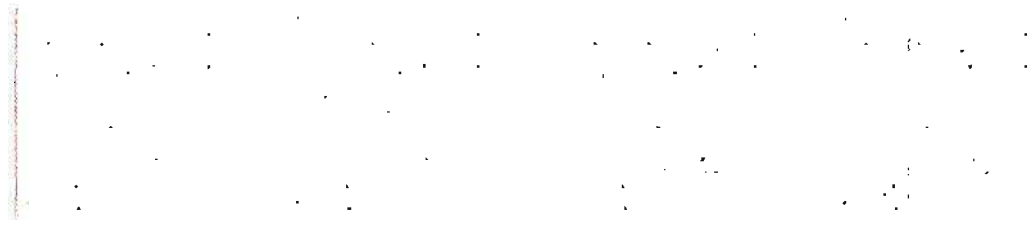
Figure 2.3: Barnes and Hut Grouping

In order to explain the Barnes and Hut algorithm, we have depicted this scheme in 2D (as in [Springel et al., 2001]). The original square (root node) is divided into four smaller squares (children) by halving the length of each side of the square. This process is continued until each node contains at most a single particle. It is not necessary to store empty nodes.

GADGET employs a number of options for the time step value. These include time steps which depend on the velocity scale, the gravitational force softening or the local density, as well as a combination of these properties.

2.3.4 Periodic Boundary Conditions

Periodic boundary conditions are implemented using an Ewald Summation Technique [Hernquist et al., 1990]. Each node in the tree is mapped onto the position of its closest periodic image. If the multipole expansion of the node is sufficiently accurate, then the partial force attributed to that node is calculated as discussed in section 2.3.1. However, there is an additional force, exerted by all of the periodic images of the node, which must still be added to this partial force. This is done by means of the Ewald technique. Let x be the co-ordinate of the point at which we wish to evaluate the force, relative to a node of mass M. The additional acceleration due to the periodic images is given by

$$
\begin{aligned}
a_c(x) = M \Bigg\{ & \frac{x}{|x|^3} - \sum_{n} \frac{x - nL}{|x - nL|^3} \times \Bigg[\text{erfc} \left(\alpha |x - nL| \right) \\
& + \frac{2\alpha |x - nL|}{\sqrt{\pi}} \exp \left(-\alpha^2 |x - nL|^2 \right) \Bigg] \\
& - \frac{2}{L^2} \sum_{h \neq 0} \frac{h}{|h|^2} \exp \left(-\frac{\pi^2 |h|^2}{\alpha^2 L^2} \right) \sin \left(\frac{2\pi}{L} h \cdot x \right) \Bigg\}
\end{aligned}
\tag{2.12}
$$

where n and h are integer triplets, L is the box size and α is an arbitrary number. Springel et al. [2001] have shown that good convergence is obtained for $\alpha = \frac{2}{L}$, summed over $|n| < 5$ and $|h| < 5$. In the same manner we can express the additional potential experienced as

$$\phi_c(\mathbf{x}) = M\left\{ \frac{1}{\mathbf{x}} + \frac{\pi}{\alpha^2 L^3} - \sum_{\mathbf{n}} \frac{\mathrm{erfc}(\alpha|\mathbf{x} - \mathbf{n}L|)}{\mathbf{x} - \mathbf{n}L} \right.$$
$$\left. - \frac{1}{L} \sum_{h \neq 0} \frac{1}{\pi|\mathbf{h}|^2} \exp\left(-\frac{\pi^2|\mathbf{h}|^2}{\alpha^2 L^2} \right) \cos\left(\frac{2\pi}{L}\mathbf{h} \cdot \mathbf{x} \right) \right\}. \quad (2.13)$$

GADGET tabulates the correction fields $\mathbf{a}_c(\mathbf{x})/M$ and $\phi_c(\mathbf{x})/M$, following the approach described by Hernquist et al. [1990]. This significantly reduces computation time as the fields only need to be determined once.

2.3.5   Parallelisation

The parallel version of GADGET uses the standard Message Passing Interface (MPI) in which the user is responsible for the control of communication between processors. MPI is a flexible and portable communication scheme which allows GADGET to run on a variety of machines.

When writing parallel code the two most important considerations are ensuring that there is an even distribution of data between the processors and optimising efficient communication between the processors.

To distribute the data of a simulation GADGET uses spatial domain decomposition, this is done by means of the orthogonal recursive bisection algorithm [Dubinski, 1996]. The domain is divided along one of the spatial directions (e.g. the x-axis) and the processors are then split into two groups, each group concerned with one section of the domain. Particles are exchanged between processors until each processor contains only the particles that are in their section of the domain. The domain will then be divided

Domain Decomposition

Processor 1   Processor 2   Processor 3   Processor 4

Individual Tree Construction
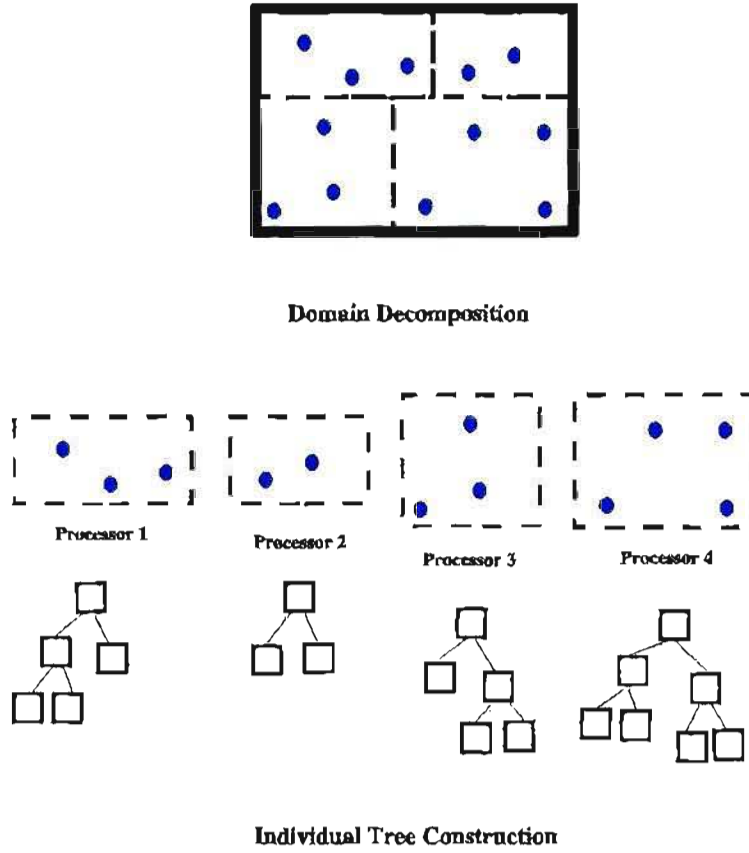
Figure 2.4: Domain Decomposition

This figure is a 2D representation of the domain decomposition implemented by GADGET (as in [Springel et al., 2001]). The domain is split along spatial directions, each processor is responsible for a section of the domain. Each processor then constructs a tree for the particles included in that section.

along another spatial direction. This subdividing of the domain continues until only one processor remains in each group. That is, one processor is solely responsible for each section of the domain. This method is illustrated in figure 2.4. In choosing where to divide the domain initially, it is important to balance the workload of the processors involved. This algorithm restricts the number of processors used in a simulation to a power of two.

For GADGET to achieve efficient work load balancing the domain decomposition should be implemented to ensure that the time taken for the tree walk of each processor, in each time step, is similar. GADGET ensures this by measuring the number of

particle-node interactions from each section of the domain and tries to keep this number similar on each section of the domain. GADGET keeps track of the computational cost of each particle by recording the number of node-particle interactions for each node. Each particle is then, according to this computational cost, assigned a weight factor. These are then taken into account when deciding on the division of the domain.

Table 2.1 shows a comparison of the time taken for the 32^3 test simulation to run on four and eight processors including the amount of time (in seconds) spent in various aspects of the code for these runs. Time spent on writing snapshot files has not been included as this is a negligible fraction of the total time. In this table 'miscellaneous' refers to the time taken by the code in particle prediction, updating of the timestep and time line as well as the time taken to measure the tree performance. The most time consuming task is that of computing the gravitational forces. As one would expect, the time spent in communication is increased when eight processors are used while the total computation time is almost halved by doubling the number of processors.

Parallelisation: Time breakdown				
	Four Processors		*Eight Processors*	
Parameter	Total time (s)	%	Total time (s)	%
Total	167.7	100	89.8	100
Gravity	138.4	83.5	68.8	76.6
Tree Walks	96.1	57.3	44.8	50.0
Tree construction	11.0	6.6	4.6	5.1
Communication and summation	1.5	0.9	3.9	4.3
Work load imbalance	13.3	7.9	5.0	5.6
Domain decomposition	18.8	11.2	14.4	16.0
Potential computation	6.7	4.0	3.4	3.8
Miscellaneous	3.8	2.3	3.2	3.6

Table 2.1: Computational Time Breakdown

This table (similar to one produced by Springel et al. [2001]) shows the amount of time taken by the cluster in the various sections of the code run on four and eight processors respectively. Time is given in seconds as well as relative time as a percentage. Time taken for the writing of snapshots is negligible and therefore not listed. Miscellaneous refers to the time taken for particle prediction, updating of timestep and time line and for diagnostics. Most time is spent on the computation of gravitational forces.
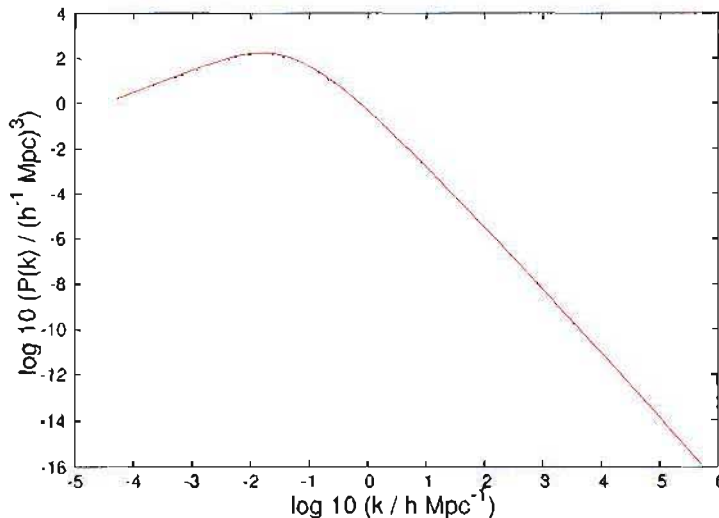
Figure 2.5: Power Spectrum
The initial power spectrum of density fluctuations in our simulation at a redshift of z ~ 45, as generated by GRAFIC.

2.4 Initial Conditions

It is often assumed that the density fluctuations in the universe result from quantum fluctuations which are greatly amplified during an inflationary phase early in the universe. A generic prediction from inflationary models is that the fluctuations are Gaussian and the initial power spectrum of density fluctuations is given by a power law, $P_0(k) \propto k^n$, where n ~ 1 [Kolb and Turner, 1993]. As the universe moves from a radiation dominated to a matter dominated phase, fluctuations begin to grow significantly and the power spectrum, $P(k)$, becomes modified in a way that depends on the density of dark matter. Bardeen et al. [1986] give the transfer function T (where $P(k)$ = $P_0(k)$ T) for a universe that is dominated by cold dark matter (see equation 2.14). The normalisation of the spectrum is obtained from observations of the Cosmic Microwave Background. To set initial particle positions and velocities such that they are consistent with CDM expectations and CMB observations we use the COSMICS package. COSMICS (Cosmological Initial Conditions and Microwave Anisotropy Codes) is a package of Fortran programs written by Ma and Bertschinger [1995]. From this set of programs we have used the GRAFIC (Gaussian Random Field Initial Conditions)

21

program to obtain the initial conditions we require for our simulation.

The initial power spectrum of density fluctuations in our simulation, as obtained using GRAFIC, is shown in figure 2.5. For this project we have adopted the concordance (standard) cosmology, described in chapter 1. Table 2.2 shows the values of the cosmological parameters used in creating our initial conditions.

The Transfer function for a cold dark matter universe is given by

$$T_{CDM}(k) = \frac{\ln(1 + 2.34\,q)}{2.34\,q} \left[1 + 3.89\,q + (16.1\,q)^2 + (5.46\,q)^3 + (6.71\,q)^4\right]^{-\frac{1}{4}} \quad (2.14)$$

where

$$q \equiv \frac{k\,\theta^{\frac{1}{2}}}{\Omega_m\,h^2\,\mathrm{Mpc}^{-1}} \quad (2.15)$$

and θ is the ratio of energy density in relativistic particles (neutrinos and photons) to that in photons. $\theta = 1$ for three flavours of relativistic neutrinos together with photons.

Parameter	Parameter Value
Ω_m	0.3
Ω_Λ	0.7
σ_8	0.9

Table 2.2: Cosmological Parameters used to Create Initial Conditions

2.5 Our Simulations

Initially, we ran a number of 128^3 particle simulations on a serial 2.8 GHz machine
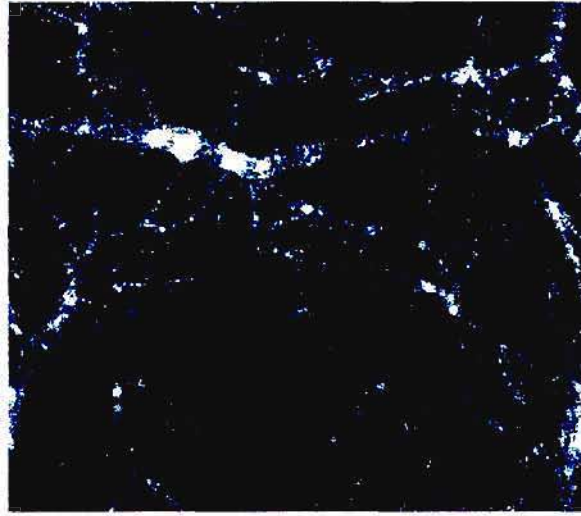
Figure 2.6: Large-Scale Structure

Illustration of a slice through our simulated box at redshift zero, showing density distributions consistent with large-scale structure observations. Further discussion on the visualisation of the simulation is given in Appendix A.

with 3.7 Gbytes of RAM. These simulations were used to familiarise ourselves with the running of GADGET and the required parameters. They were also used to explore the evolution of the mass function with redshift. The snapshots produced by a 128^3 simulation were small enough for us to store records of the simulation up to a redshift of ten. To obtain a higher resolution simulation we then ran the parallel version of GADGET on a cluster of eight 2 Gbyte machines. Doing so increased the amount of memory available, allowing us to increase our particle number to 256^3.

2.5.1   Simulation Volume

The volume of the region of space to be simulated will affect the resolution of the simulation. Decreasing the length of the box will increase the resolution for a given number of particles. However, since we are employing periodic boundary conditions, we need to be aware of a minimum box size for which the simulations can be considered reliable. The box must be large enough to ensure that perturbations which occur on scales comparable to the box length are still linear today. Power et al. [2003] show that

23

the minimum box length required for reliable periodic simulations is approximately 32.5 h^{-1} Mpc.

We have chosen to simulate a cube of length 50 h^{-1} Mpc, which is sufficiently large to produce reliable periodic simulations [Power et al., 2003].

2.5.2 Particle Mass

We can express the total mass enclosed in a simulated box as $\Omega_m \times \rho_{crit} \times$ volume where ρ_{crit} (the density of the universe) is $2.7755 \times 10^{11} h^2 M_\odot$ Mpc^{-3}. Once we know the total mass being simulated, the mass of an individual particle is easily determined by dividing the total mass by the number of particles.

$$m_{\text{particle}} = 8.3265 \times 10^{10} \ h^2 M_\odot \, \text{Mpc}^{-3} \, \frac{\text{Volume} \, (h^{-1} \text{Mpc})^3}{\text{Number of particles}}. \tag{2.16}$$

The mass of the particles depends on both the number of particles and the volume of the simulations. The smaller we are able to make our particle mass, the higher the resolution of the simulation.

This choice of particle number and volume means that, in our simulation, each dark matter particle has a mass of about $6 \times 10^8 \ h^{-1}$ solar masses. The simulation provides a large sample of halos with the resolution required for figure rotation measurements.

2.5.3 Force Softening

Force softening, introduced in 2.1.1, is essential to prevent two body collisions from driving the simulation. Merritt [1996] discusses the optimal force softening for the direct summation technique, describing the choice of the force softening as a "bias-variance tradeoff". Using a value of the force softening parameter which is too small will result in an estimate that is too noisy. However, having too large a value for

Parameter	Parameter Value
$N_{particles}$	256^3
Box Length	$50 \ h^{-1}$ Mpc
$M_{particle}$	$6.2 \times 10^8 \ h^{-1} \ M_\odot$
Force Softening	$30 \ h^{-1}$ kpc
Initial Redshift	55

Table 2.3: Simulation Parameters

the softening parameter results in "the systematic misrepresentation of the force due to failure to resolve real features with scale lengths less than the softening length". Athanassoula et al. [2000] extended this work, discussing the optimal force softening for different mass distributions as well as the effects of using a tree code.

Guided by studies of Athanassoula et al. [2000] we have used a force softening of $30 \ h^{-1}$ kpc to prevent numerical instability. The parameters chosen for our simulation are summarised in table 2.3. The resulting structure formed in our simulation is depicted in figure 2.6. This figure shows a projected slice through our simulated box at a redshift of zero, clearly visible are filaments and voids. Further discussion on the visualisation of the simulation is given in Appendix A.

2.5.4 Choosing a Time Step

The choice of time step is an important one. Using a large time step allows the simulation to run very quickly as less computation is required, however if the time step becomes too large accuracy is lost. It is essential to ensure that the timestep is small enough to follow the trajectory of the simulated particles reliably.

GADGET employs a number of options for the time step value. These include time steps which depend on the velocity scale, the gravitational force softening or the local density as well as a combination of these. The time steps dependent on dynamical

properties of the simulation require more memory and we have, for this reason, opted to use a simple timestep which is inversely proportional to the expansion factor, a. We have chosen a conservative proportionality constant to ensure sufficient accuracy.

Chapter 3

Methodology II: Analysis

3.1 Identifying Halos

A halo is defined to be a grouping of ten or more dark matter particles. Groups are found using a friends-of-friends algorithm [Davis et al., 1985], whereby a particle of interest is selected, then a search for any other particles within a specified distance from this particle is conducted. If a particle is found, the search is continued around that particle. This is repeated until no further particles can be added to the group. The search distance is known as the linking length. To identify groups we have used the common convention of choosing a linking length of 0.2 times the mean interparticle spacing, a value which has been shown empirically to give good results (larger values result in all particles being associated with a single group and smaller values result in no groups being identified).

Figure 3.1 shows a projected slice through our 128^3 simulation at redshift zero. The gray scale shows the large-scale structure, while the halos identified by the group finder are shown in colour.

Snapshot files containing the position and velocity of every particle are written out at specified redshifts. At each redshift, we create a catalogue of halos identified from the

Figure 3.1: Identified Halos

A projected slice through our simulation at redshift zero. The gray scale shows the large-scale structure, while the halos identified by the group finder are shown in colour (assigned arbitrarily).

snapshot. Each entry in the catalogue contains the following information about the halo :

- The number of particles contained within the halo.

- The x, y, z position of the central (the most gravitationally bound) particle.

- The virial radius (the distance from the central particle at which the dark matter overdensity drops below a constant factor times the background density).

- The virial mass (the mass contained within the virial radius).

- The circular velocity which can be found using

$$V_c = \left(\frac{G \, M_{vir}}{R_{vir}} \right)^{\frac{1}{2}} . \tag{3.1}$$

3.2 Merger Trees

To follow halo properties with redshift, we need to be able to associate each halo with its progenitor halo at a previous timestep. This is done with merger trees using code developed by Kauffmann and White [1993]. Merger trees describe the way in which structure builds up over time. Since ΛCDM predicts that structure forms hierarchically (small structures merge to form larger structures) we expect that each halo may have several progenitors but only one descendant.

A halo at redshift z_{i-1} is said to be a progenitor of a halo at redshift z_i if, and only if, two conditions are satisfied:

1. A progenitor halo at z_{i-1} must contribute at least half of its particles to the halo at z_i and

2. the central particle of the progenitor halo at z_{i-1} must be contained within the halo at z_i

It may happen that a halo identified at one redshift cannot be associated with any progenitor halo. In this case, the halo cannot be traced any further back in time. This may happen for a number of reasons. In a hierarchial structure formation scenario, small groups form first and merge into larger groups. It may happen that, as one moves backwards in time, the halo falls below the 10 particle cutoff used to define a halo. A higher resolution simulation is required to trace this halo back in time.

To follow the progress of a halo, we need to know the central particle and the number of the halo we are following at each redshift. Using the merger trees, we are able to follow the progress of a halo and its constituent particles over time.

3.3 Rigid Body Rotation

For figure rotation analysis, we model each halo as a rigid body. A rigid body can be defined as a collection of particles whose relative distances remain fixed. This is

an idealised model as the constituent particles within the halo are free to move and will undergo some relative motion. Typically the scale of this motion is microscopic in relation to the rotation of the body, and the relative motion of the particles is ignored.

In Appendix C, we define the inertia tensor as

$$I_{ij} = \sum_{\alpha} m_{\alpha} \left[\delta_{ij} \sum_{k} x_{\alpha,k}^2 - x_{\alpha,i} x_{\alpha,j} \right]$$

where $x_{\alpha,1}$, $x_{\alpha,2}$, $x_{\alpha,3}$ are the three coordinates of the αth particle and m_{α} is the mass of the αth particle.

Expressions for kinetic energy and angular momentum are then given by

$$T_{\text{rotation}} = \frac{1}{2} \sum_{i,j} I_{i,j} \omega_i \omega_j \tag{3.2}$$

$$L_i = \sum_{j} I_{ij} \omega_j \tag{3.3}$$

where ω is the angular velocity of the rotating axes. Expanding our definition for the Inertia tensor (equation 3.2) we have

$$\mathbf{I} = \sum_{\alpha} m_{\alpha} \left\{ \begin{array}{ccc} x_{\alpha,2}^2 + x_{\alpha,3}^2 & - x_{\alpha,1} x_{\alpha,2} & - x_{\alpha,1} x_{\alpha,3} \\ - x_{\alpha,2} x_{\alpha,1} & x_{\alpha,1}^2 + x_{\alpha,3}^2 & - x_{\alpha,2} x_{\alpha,3} \\ - x_{\alpha,3} x_{\alpha,1} & - x_{\alpha,3} x_{\alpha,2} & x_{\alpha,1}^2 + x_{\alpha,2}^2 \end{array} \right\} . \tag{3.4}$$

From this we can clearly see that the Inertia Tensor is symmetric and has only six independent elements.

The diagonal elements (I_{11}, I_{22}, I_{33}) are known as the *moments of inertia* about the

x_1, x_2, x_3 axes respectively, while the negatives of the off-diagonal elements are known as the *products of inertia*.

The diagonalisation of the inertia tensor results in significant simplifications for the expressions of kinetic energy and angular momentum. If we could write $I_{ij} = I_i \delta_{ij}$ the inertia tensor would be

$$\mathbf{I} = \left\{ \begin{array}{ccc} I_1 & 0 & 0 \\ 0 & I_2 & 0 \\ 0 & 0 & I_3 \end{array} \right\}. \tag{3.5}$$

We could then express the kinetic energy and angular momentum as

$$\begin{aligned} T_{rot} &= \tfrac{1}{2} \sum_{i,j} I_i \delta_{ij} \omega_i \omega_j = \tfrac{1}{2} \sum_i I_i \omega_i^2 \\ L_i &= \sum_j I_i \delta_{ij} \omega_j = I_i \omega_i. \end{aligned} \tag{3.6}$$

In order to diagonalise $\mathbf{I}$ we need to find a set of body axes for which the products of inertia are all zero. The axes, which satisfy this condition, are known as the *principal axes*.

Consider a body which rotates about a principal axis with both the angular momentum and velocity of this body directed along this principal axis. We can write

$$\mathbf{L} = \mathbf{I}\boldsymbol{\omega}, \tag{3.7}$$

or, if we expand this into its components

$$\begin{aligned} L_1 &= \mathbf{I}\omega_1 = I_{11}\,\omega_1 + I_{12}\,\omega_2 + I_{13}\,\omega_3 \\ L_2 &= \mathbf{I}\omega_2 = I_{21}\,\omega_1 + I_{22}\,\omega_2 + I_{23}\,\omega_3 \\ L_3 &= \mathbf{I}\omega_3 = I_{31}\,\omega_1 + I_{32}\,\omega_2 + I_{33}\,\omega_3. \end{aligned} \tag{3.8}$$

Rearranging the components of the angular momentum vector gives

$$(I_{11} - I)\omega_1 + I_{12}\,\omega_2 + I_{13}\,\omega_3 = 0$$
$$I_{21}\,\omega_1 + (I_{22} - I)\,\omega_2 + I_{23}\,\omega_3 = 0 \tag{3.9}$$
$$I_{31}\,\omega_1 + I_{32}\,\omega_2 + (I_{33} - I)\,\omega_3 = 0\,.$$

This is of the form

$$(I - I\mathbf{1}) \cdot \boldsymbol{\omega} = 0\,. \tag{3.10}$$

For figure rotation analysis, we determine I from the simulations and then obtain I and ω (the eigenvalues and eigenvectors) using Jacobi transformations.

3.4 Procedure

We have identified halos (groups of ten or more particles) in the redshift zero snapshot using a friends-of-friends group finder for N-body simulations developed by the NASA HPCC ESS group at the University of Washington. Using the positions of the particles contained within the halo we are able to calculate the Inertia Tensor and, hence, the principal axes of the halo of interest at each time step.

3.4.1 Calculating the Inertia Tensor

In the definition of the Inertia tensor given in equation 3.2, the particles furthest from the centre of mass are the most heavily weighted. Substructure in the outer regions of the halo (such as a satellite galaxy which has recently fallen into the halo) then affects the calculation of the Inertia Tensor significantly. In order to reduce this effect, we have weighted each particle by $\frac{1}{r^2}$ as suggested by Bailin and Steinmetz [2004]. To minimise the effect of substructure we use the modified Inertia Tensor given by

$$\tilde{I}_{ij} = \sum_k \frac{r_{k,i}\, r_{k,j}}{r_k^2}. \tag{3.11}$$

3.4.2 Determining the Principal Axes

Using Jacobi Transformations, we are able to extract the eigenvalues and eigenvectors of the inertia tensor. Jacobi transformations are a sequence of orthogonal similarity transformations. Each of the off diagonal matrix elements is eliminated by one of these transformations. Successive transformations may unset the off diagonal zeros, but these continue to decrease until they are machine precision zero. The resulting diagonal elements are the eigenvalues of the system. Keeping track of the product of the transformations results in a matrix containing the eigenvectors. The eigenvectors are known as the *principal axes*, and can be thought of as preferred directions of rotation.

33

Each of the eigenvalues corresponds to a moment of inertia about one of the principal axes and is termed a *principal moment of inertia*.

An algorithm implementing Jacobi transformations, taken from Numerical Recipes [Press et al., 1992], was used to extract the eigenvalues and eigenvectors of the modified Inertia Tensor of the halos for each of the recorded redshifts. (A list of the redshifts used in this analysis is given in table 3.1.)

Reflection symmetry of the principal axes means that we cannot measure true rotation angles greater than 90 degrees between successive snapshots. To prevent erroneous measures of this nature, we have taken the absolute value of the eigenvector in all calculations. Fortunately, our results show that the observed pattern speeds are much too low for this to be an area of concern.

3.4.3 Measuring the Figure Rotation

Dubinski [1992], noted that the 'tumbling' period of a halo could be found by comparing the principal axes of the halo over several time intervals. For a halo tumbling about a fixed axis, the angle of rotation, θ is given by

$$\cos\theta = \frac{\cos A + \cos B + \cos C}{2} \tag{3.12}$$

where A, B and C represent the angles between the corresponding eigenvectors over a given time interval.

An alternative method, suggested by Bailin and Steinmetz [2004], is a plane fitting approach, illustrated in figure 3.2. This method involves fitting a plane to the principal axes of the halo of interest. This is done by considering the principal axes of the halo over several time steps, then solving for the plane z = ax + by that best fits these axes. Once the plane has been determined, measuring the amount of rotation in the plane is
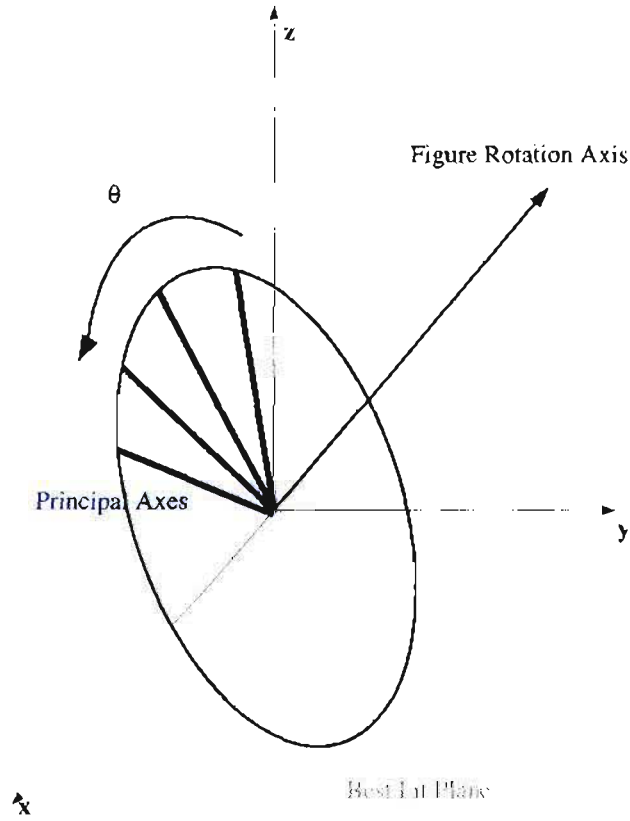
34

Figure 3.2: Plane Fitting

Following Bailin and Steinmetz [2004] the best fit plane is calculated from the principal axes of the halo over several time steps. The principal axes are then fit to this plane, and the rotation (θ) over these time steps is measured.

straight forward. The principal axis is projected onto the plane at each time step and the angle between the projected principal axes over a time interval gives the rotation of the halo.

To determine the rotation of the halo, we have followed the plane fitting approach suggested by Bailin and Steinmetz [2004]. The principal axes are projected onto the best fit plane. The angle between consecutive redshifts gives the rotation of the halo. We have then used linear regression to find the best fit linear relation for this figure rotation, the slope of this fit determines the pattern speed of the halo.

Redshift	Scale Factor
0.50	0.67
0.30	0.77
0.20	0.83
0.10	0.91
0.08	0.93
0.05	0.95
0.03	0.97
0.02	0.98
0.01	0.99
0.00	1.00

Table 3.1: Recorded Redshifts

A list of the redshifts for which the positions and velocities of each particle were recorded and considered in determining the rotation of the halo. The scale factor $a(t) = \frac{1}{1+z}$.

Chapter 4

Results and Discussion

In this chapter, we test our simulations by comparing the mass function and the distribution of the spin parameters computed from our simulated halos with results from the literature. We then discuss the effects of substructure on our analysis and describe the process of eliminating recently merged halos. Finally, we discuss the figure rotation of the remaining, undisturbed, halos.

4.1 Evolution of Structure

Figure 4.1 shows how structure formation occurs within our simulated box. Initially, slight overdensities are visible. These can be seen to be collapsing under gravity to form the large-scale structure we observe today. Positions of the particles are given in co-moving coordinates; these are the physical coordinates divided by the scale factor. Co-moving coordinates do not, therefore, increase with the expansion of the universe.

4.2 Mass Function

It is difficult to compare simulations with observations directly as luminous matter is related to dark matter in a complicated way. It is thus useful to compare our data with analytic results as well as other simulations in order to verify that the simulations are credible. The first step in doing this will be to compare our simulated mass function with that of Jenkins et al. [2001].
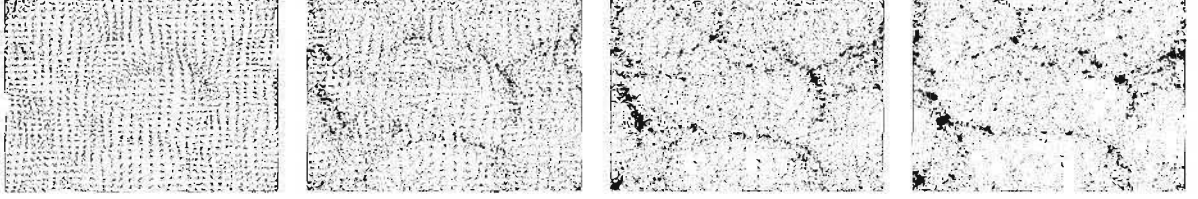
Figure 4.1: Structure Evolution in Simulated Box

A projected slice through the simulated box. Redshift decreasing to the right. In the first image one can see small perturbations to a regular lattice. The particles fall together, under the influence of gravity, to form the large-scale structure we see today. The last image shows voids and filaments typical of those we observe. Positions are in co-moving coordinates.

The mass function is a measure of the number of halos as a function of their mass. Jenkins et al. [2001] were able to predict the mass distribution of dark halos expected in a Cold Dark Matter universe by combining the results from several N-body simulations. The fit obtained by Jenkins et al. [2001] shows excellent agreement with the theoretical predictions of the Sheth and Tormen formula [Sheth and Tormen, 1999].

The mass function obtained from our simulation is shown in figure 4.2. This figure is a log plot of the number of halos as a function of their mass in the 50 h^{-1} Mpc^3 region of our simulation, at a redshift of zero. The solid line is the fit obtained by Jenkins et al. [2001]. We have found that our mass function agrees well with that of Jenkins et al. over the range of halos simulated (from 10^{11} to 10^{14} solar masses).

Typically, galaxies are thought to contain $10^8 - 10^{13}M_\odot$, groups of galaxies $\sim 10^{13}M_\odot$ and clusters of galaxies $10^{14} - 10^{15}M_\odot$. The majority of our halos are galaxy- or group-sized halos, however a few small clusters have been detected.

We have also considered the mass function at several other redshifts; these results are shown in figure 4.3. This figure shows the mass function from our simulation at redshifts of 0 (blue line), 0.5 (green line) and 1.5 (red line). We can clearly see that as the redshift decreases, the number of small halos decreases, while the number of large
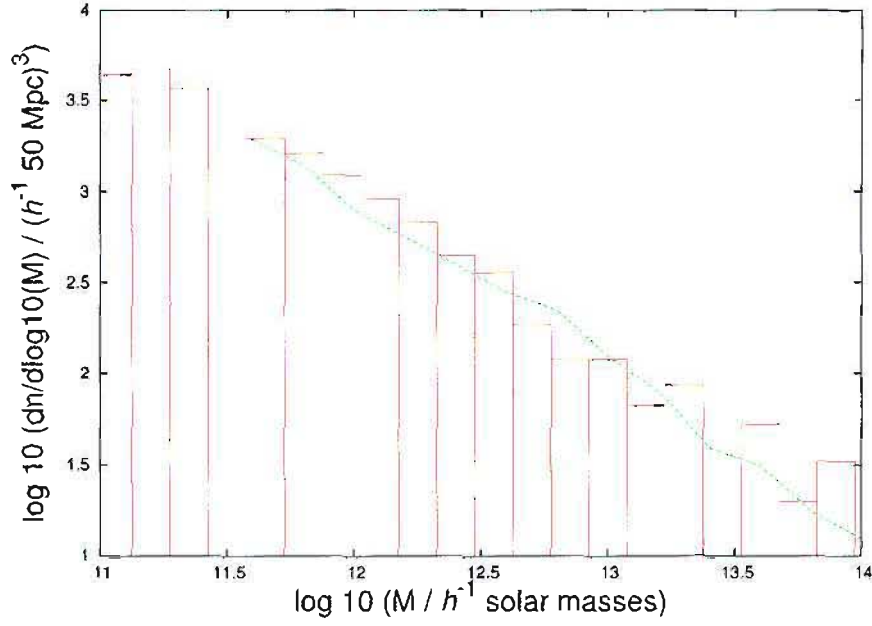
Figure 4.2: Mass Function

The number of halos as a function of the halo mass in the simulated 50 h^{-1} Mpc ^{3} region at redshift zero. The line is the fit obtained by Jenkins et al. [2001].

halos increases. This is because, with time, the smaller halos merge together forming larger structures as predicted by hierarchical structure formation.

We have also calculated the mass function for our smaller 128^3 (2 097 152) particle simulation. In this simulation we have recorded the halo attributes at higher redshifts. Figure 4.4 shows the mass function at redshifts of 10, 7, 5 and 0.

In figure 4.4 we notice that as redshift decreases, more and more halos (small and large) are being formed. During the matter dominated era (see section B.4) structure forms as the result of the collapse of overdensities under gravity. If we look at the same plot for more recent times (figure 4.3) we notice that the number of smaller halos decreases as redshift decreases. This is because the universe is currently dominated by dark energy (Λ). During the Λ-dominated era structure formation stagnates, fewer small halos are being formed and they merge to form larger structures.

Figure 4.3: Evolution of Mass Function (z = 0, 0.5, 1.5)

The number of halos as a function of the halo mass in the simulated 50 h^{-1} Mpc ^{3} region, shown for redshifts 0(blue line), 0.5(green line) and 1.5(red line).

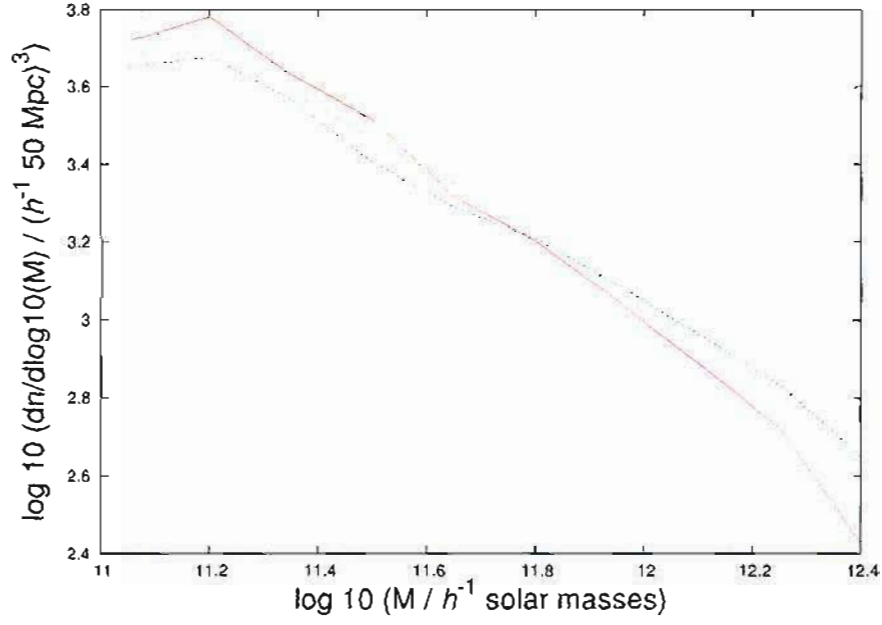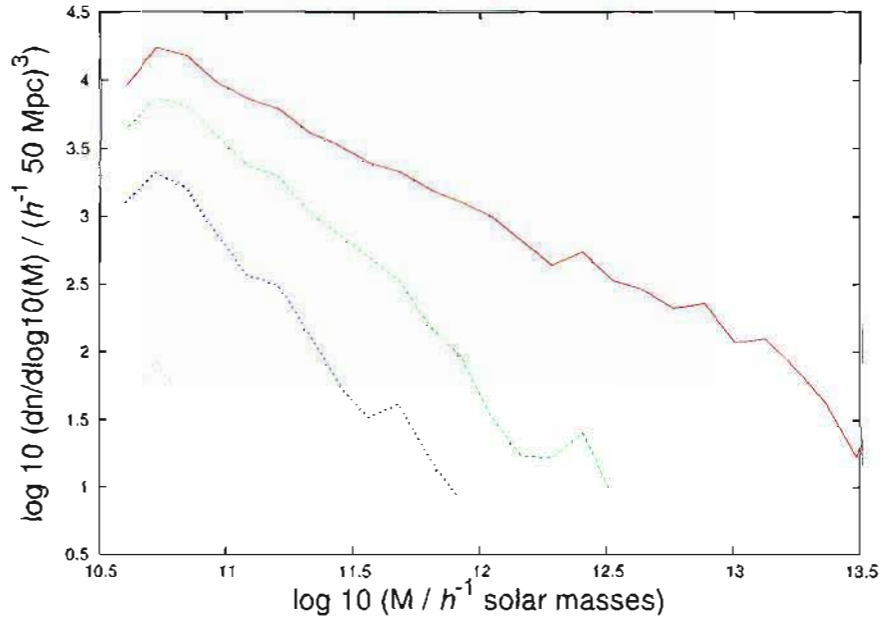Figure 4.4: Evolution of Mass Function (z = 0, 5, 7, 10)

The number of halos as a function of the halo mass in the simulated 50 h^{-1} Mpc ^{3} region. The different curves correspond to different redshifts. From top to bottom, z = 0, 5, 7, 10.

4.3 Angular Momentum

As a second test of the reliability of our simulations, we have compared the distribution of the spin parameter computed from our simulated halos with results in the literature. The angular momentum of a rigid body is discussed in detail in appendix C where we give the definition for angular momentum (equation C.8) as

$$\mathbf{L} = \sum_{\alpha} \mathbf{r}_{\alpha} \times \mathbf{p}_{\alpha} \,.$$

The angular momentum for the halo as a whole can be expressed as the sum of the angular momentum contributed by each individual particle. The angular momentum of the halo can be rewritten as

$$\mathbf{J} = m_{\alpha} \sum_{\alpha=1}^{N} \mathbf{r}_{\alpha} \times \mathbf{v}_{\alpha} \,, \tag{4.1}$$

where $\mathbf{r}_{\alpha}$ and $\mathbf{v}_{\alpha}$ are the position and velocity of the αth particle with respect to the centre of mass of the halo. Knowing the angular momentum of the individual particles allows us to calculate the angular momentum of the halo as a whole. Peebles [1969] define the dimensionless spin parameter λ as

$$\lambda = \frac{J \, \|E\|^{\frac{1}{2}}}{G \, M^{\frac{5}{2}}} \,. \tag{4.2}$$

In this equation, M is the total mass of the halo, J is the total halo angular momentum, E is the energy of the halo and G is Newton's Gravitational Constant. We will, however, use the more convenient expression for the spin parameter as defined by Bullock et al. [2001] as
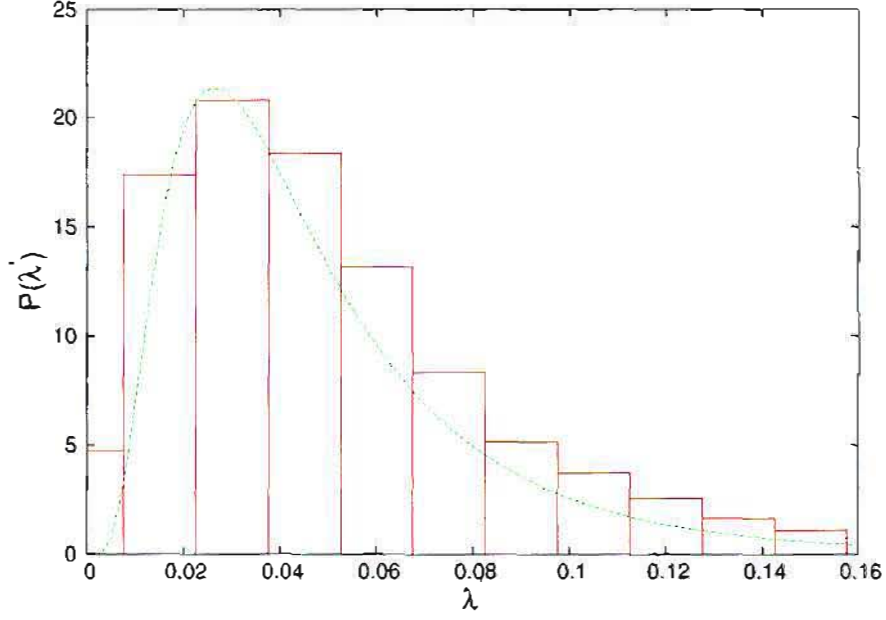
Figure 4.5: Spin Distribution

This figure shows the distribution of the dimensionless spin parameter λ' for all simulated halos containing at least 200 particles, together with the log normal distribution given by equation 4.4 ($\lambda'_0 = 0.040 \pm 0.002$ and $\sigma = 0.64 \pm 0.05$).

$$\lambda' \equiv \frac{J}{\sqrt{2}\, M V R} \tag{4.3}$$

to calculate the spin parameter of each of our simulated halos. This expression describes the spin parameter for a sphere of radius R, where M is the mass contained within the sphere, J is the angular momentum of the sphere, and V is the circular velocity at the radius R (equation 3.1). Equation 4.3 reduces to equation 4.2 when R is taken to be the virial radius of a truncated singular isothermal halo, a model which describes the density distributions of halos fairly well.

4.3.1 Spin Distribution

Barnes and Efstathiou [1987] studied the origin of angular momentum in N-body simulations. They found the dimensionless spin parameter to have a median value of around 0.05. More recently Bullock et al. [2001] analysed the spin distribution of a sample of

about 500 halos with masses greater than $1 \times 10^{12} \ h^{-1}M_\odot$. They found that the spin distribution was well fit by the log normal distribution

$$P(\lambda') = \frac{1}{\lambda'\sqrt{2\pi}\sigma} \ \exp\left(-\frac{\ln^2\left(\frac{\lambda'}{\lambda_0'}\right)}{2\sigma^2}\right)$$ (4.4)

and determined their best fit values of λ_0' and σ to be 0.035 $\pm$ 0.005 and 0.50 $\pm$ 0.03 respectively, thus agreeing with the value given by Barnes and Efstathiou [1987]. Figure 4.5 shows the distribution of the spin parameter found in our simulation. The spin parameter was calculated for all simulated halos which have a mass greater than $10^{11} \ h^{-1}M_\odot$. The curve is the log normal distribution given by equation 4.4 with best fit values of $\lambda_0' = 0.040 \pm 0.002$ and $\sigma = 0.64 \pm 0.05$. We have found that the our best fit value for λ_0' agrees well with the values obtained by Barnes and Efstathiou [1987] and Bullock et al. [2001]. Our spin parameter has a slightly wider distribution than that found by Bullock et al. but the σ values agree within the 2 σ uncertainties. The difference is probably due to our cruder estimate of the virial radius.

All fits in this project were obtained using an implementation of the non-linear least-squares Marquardt-Levenberg algorithm.

4.4   Simulated Halos

From our simulation we have identified the 222 halos, at a redshift of zero, which contain at least 4000 particles (that is a mass of at least $2.5 \times 10^{11} \ h^{-1} M_\odot$) for further analysis. This cutoff was suggested by Bailin and Steinmetz [2004]. They used a computationally intensive bootstrapping technique to show that, as one would expect, the error in the determination of a halo's principal axes depends on the number of particles contained within that halo and the intrinsic shape of the halo. Using the bootstrapping technique, Bailin and Steinmetz [2004] also showed that it was not possible to measure the principal axes of halos with the precision required for figure rotation measurements if the halos contained fewer than 4000 particles.
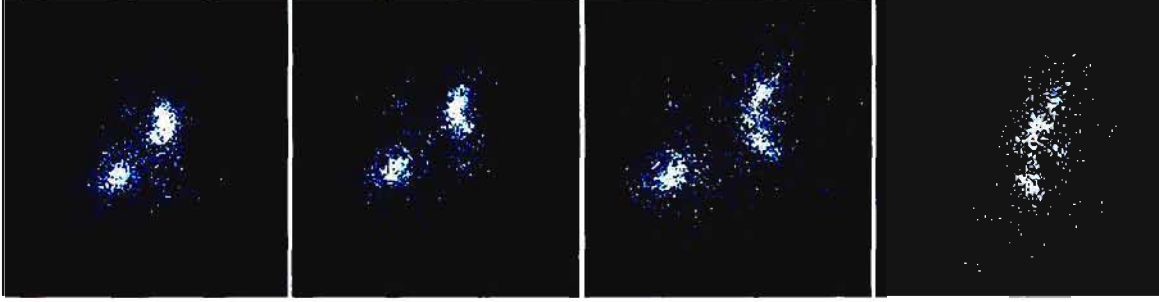
4.5   Detecting Recent Mergers

Figure 4.6: Images of a Merger

The plots above shows projected images of two halos identified as undergoing a major merger. Redshift decreasing to the right.

In this project, we were concerned with the figure rotation of undisturbed halos and, therefore, needed to eliminate those halos that had only recently undergone a merger. To do this, we consider the fraction of the particles currently contained in a halo that belong to that same halo at earlier time intervals. We are interested in how much mass mergers have contributed to the mass of the halo. If this fraction is less than 90 %, we will disregard that halo as one having recently merged. From our sample of 222 halos, 23 have been identified as having undergone a merger after $z \approx 0.05$ and have been eliminated from our sample set. Clearly, as we look further back, more and more halos will be affected by mergers. Figure 4.6 illustrates the effects of a merger. This is a sequence of projected images of a halo identified as having undergone a recent major merger.

4.6   Substructure

We have already explained the need to eliminate recently merged objects, and we have discussed the first approach used to do so. Of the remaining halos we will also discard halos that contain a significant amount of substructure. Substructure will severely affect the calculation of the inertia tensor and the precise determination of
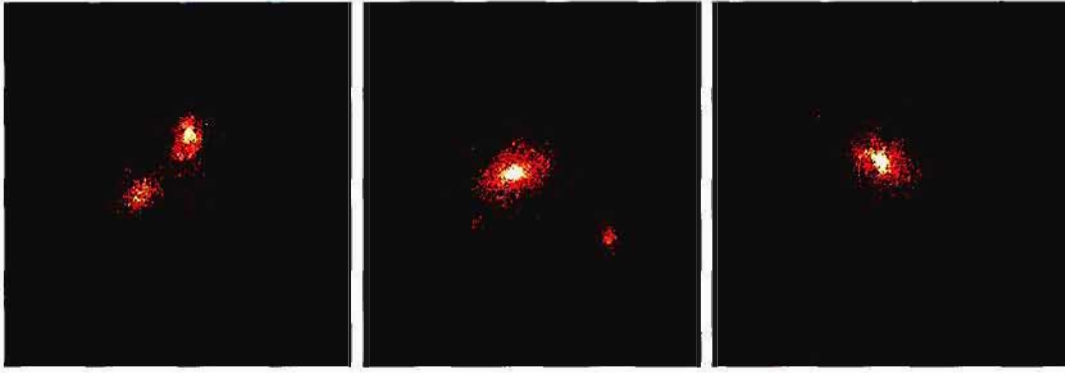
Figure 4.7: Images of Halos with Varying Amounts of Substructure
The three FITS images above show varying amounts of substructure. Left: Significant substructure. Centre: Some substructure visible at the edge of the halo. Right: An undisturbed halo. The left and central halos have been eliminated from our sample.

the principal axes (see Section 3.4.1). Figure 4.7 shows FITS images of three halos from our sample. These three halos contain different amounts of substructure. The left image clearly shows two regions of high density. In the middle image, substructure is visible in the bottom left corner of the halo. The right image shows an undisturbed halo.

To determine a qualitative measure of the amount of substructure contained within a given halo, we have plotted the mass distribution of the halos. Figure 4.8 shows a projection of the mass distribution of the three halos depicted in figure 4.7, these halos contain varying amounts of substructure. We expect the distribution of an undisturbed halo to be smooth, peaked at the centre of the halo. The presence of a secondary peak in this distribution provides evidence of substructure. If the secondary peak contains 20% of the primary peak mass, then we eliminate that halo on the basis of substructure. Since we are considering the evolution of the halos with time, we need to consider the substructure at all time intervals of interest. Applying this to our sample of halos over a period of about a gigayear, we have eliminated 123 halos on the basis of substructure. Looking further back, over about three gigayears, we expect more halos to be affected by substructure, in fact, over this period 130 halos need to be excluded from the sample. There is only a small increase in the number of affected halos over three

45

gigayears as most halos that are affected by substructure at high redshift ($z \sim 0.5$) will still be affected at recent times.

The 23 halos eliminated previously as having recently merged, would also be identified and eliminated by this method.
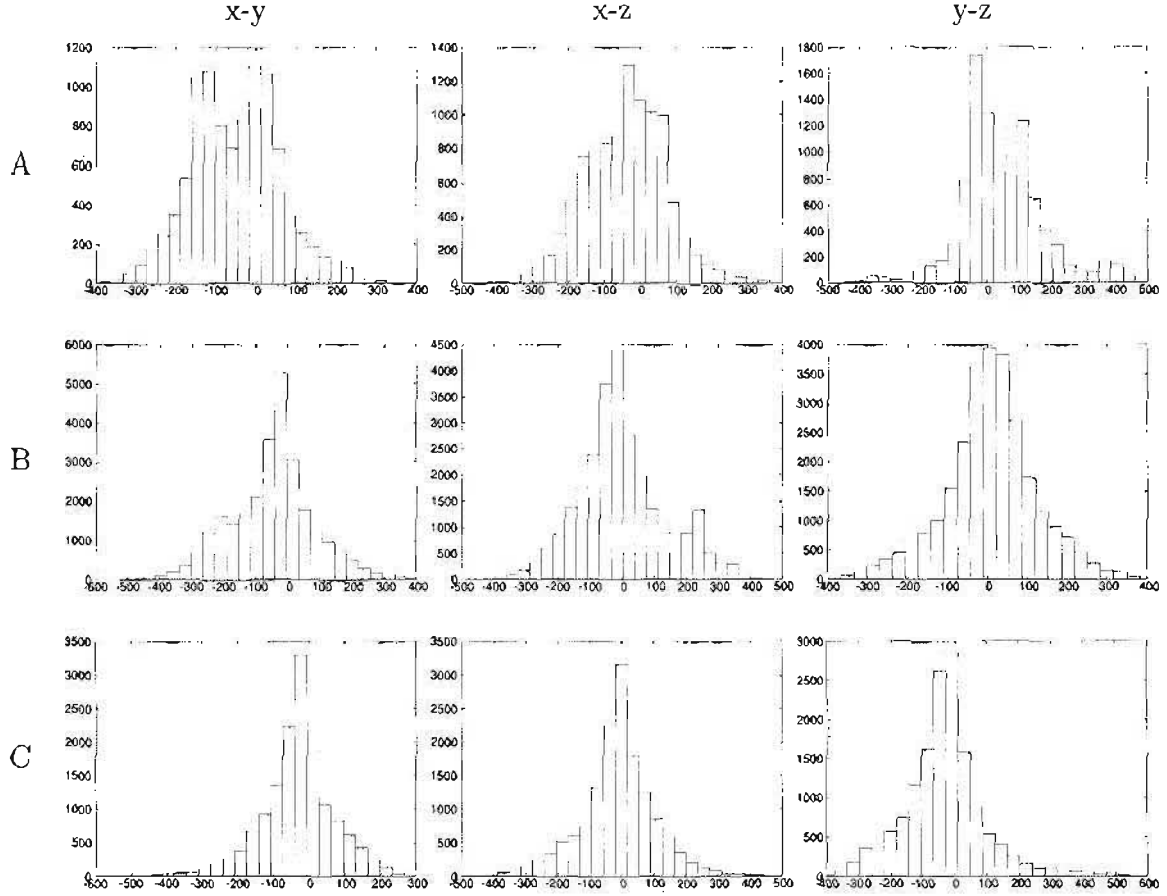
Figure 4.8: A Measure of the Amount of Substructure

Mass distributions are shown for three projections (x-y, x-z and y-z) of three halos shown in figure 4.7 (A, B, C). The horizontal axes give the distance from the central particle (h^{-1} kpc) and the vertical axes give the number of particles at that distance. The top row of images show a halo with a secondary peak containing almost as much mass as the primary peak, a clear indication of significant substructure. The second row of images are those of a halo with a secondary peak contributing 34% of the primary peak mass. Finally, the bottom row shows an undisturbed halo.
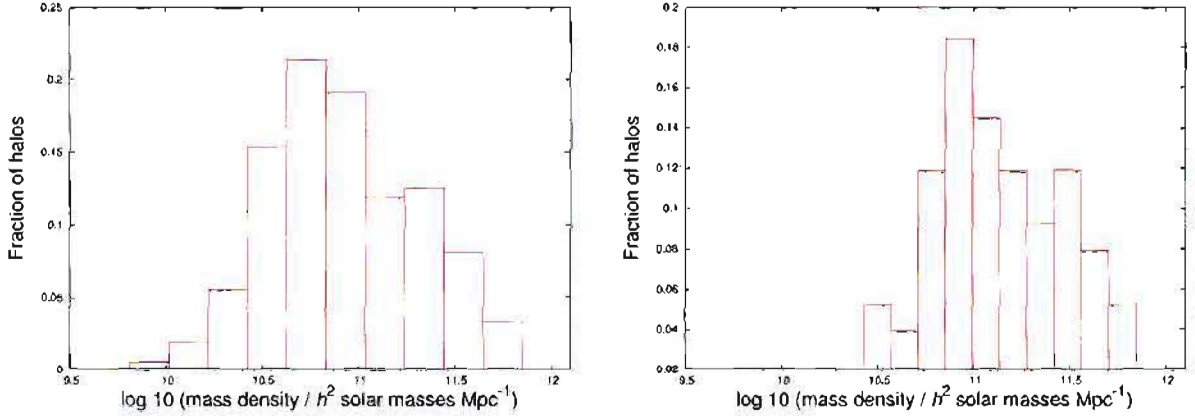
Figure 4.9: Mass Density in Surrounding Environment

These histograms show the fraction of halos versus the log of the mass density of the surrounding environment. Left: The surrounding environment of all simulated halos. Right: The environment of the halos selected for 1 gigayear analysis.

4.7 Mass Density in Surrounding Environment

In order to explore the environment of our halos, we have considered the mass density of the area surrounding the halos. To do this we have, for each halo, found the number of particles within 5 h^{-1} Mpc of the halo. The sum of the surrounding mass is then divided by the volume of a sphere with radius of 5 h^{-1} Mpc. The results are shown in figure 4.9; these are plots of the fraction of halos as a function of the log of their mass density. The left figure shows the distribution of mass density of the all halos identified from the simulation, while the right histogram shows the distribution of our sample of undisturbed halos. While the distributions cover a similar range, the undisturbed halos appear to occur in a slightly more dense than average environment. This is consistent with the results of Gottlöber et al. [2001]. They found that, for z < 1, the merger rate of cluster halos to be 3 times lower than that of isolated halos and twice as low as halos that end up in groups. With this in mind, we expect that undisturbed halos would occur in a more dense environment.

48

4.8 Figure Rotation

Finally, we have a set of 76 halos that are undisturbed over a period of a gigayear, 69 of which are unaffected by substructure over three gigayears. From this set we wish to determine firstly, whether or not there is any coherent rotation of the halo as a whole and secondly, if there is coherent rotation, a measure of the speed of this rotation. The method used to determine the rotation of each halo is discussed in section 3.4.3.

For each of the 76 undisturbed halos, we have calculated the modified inertia tensor and then used a Jacobi transformation routine to determine the principal axes of the halo at each timestep. Figure 4.10 shows one such halo together with its major axis. We have used a plane fitting technique to find the plane that best fits the set of major axes calculated for each timestep. We then projected the major axis onto the best fit plane, and measured the angle between these projected axes at each time interval. Figure 4.11 shows the orientation of the major axis of one of our undisturbed halos at redshifts 0, 0.01, 0.02, 0.03, 0.05, 0.08 and 0.1 (redshift decreasing clockwise).

Figure 4.12 shows the rotation of one of our typical undisturbed halos. The first seven panels (left to right, top to bottom) show a projection of the halo at redshifts 0, 0.01, 0.02, 0.03, 0.05, 0.08 and 0.1 (from top left) together with the halos major axis. The bottom right figure shows the rotation of the major axis as a function of time.

We have also measured the rotation of several halos using the method described by Dubinski [1992] and found that these results are similar to the ones we obtain using the plane fitting approach.
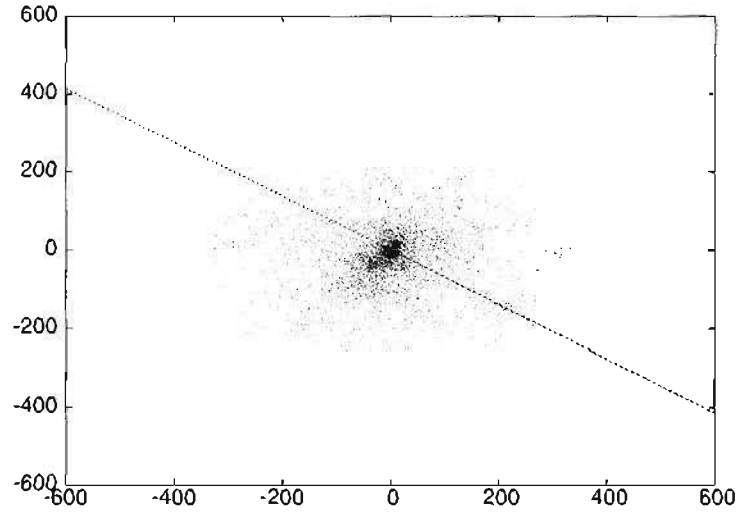
Figure 4.10: Projected Image of an Undisturbed Halo, Principal Axis Superimposed

This figure shows a projected view of an average undisturbed halo together with its major axis. The vertical and horizontal axes give the distance from the centre of the halo in h^{-1} kpc.
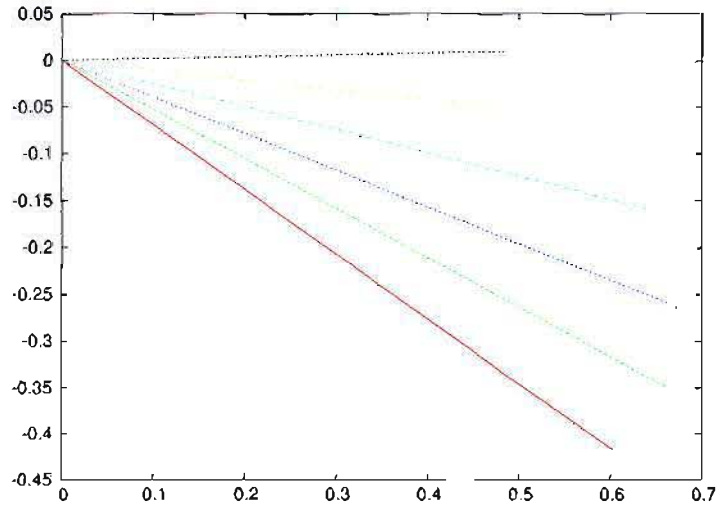

Figure 4.11: Rotation of the Principal Axis with Time

The orientation of the major axis of an undisturbed halo. Different colours correspond to the major axis at different times (redshift decreasing clockwise). This halo has undergone a rotation of approximately 0.5 radians over a period of one h^{-1} gigayear.

Figure 4.12: Figure Rotation of a Halo
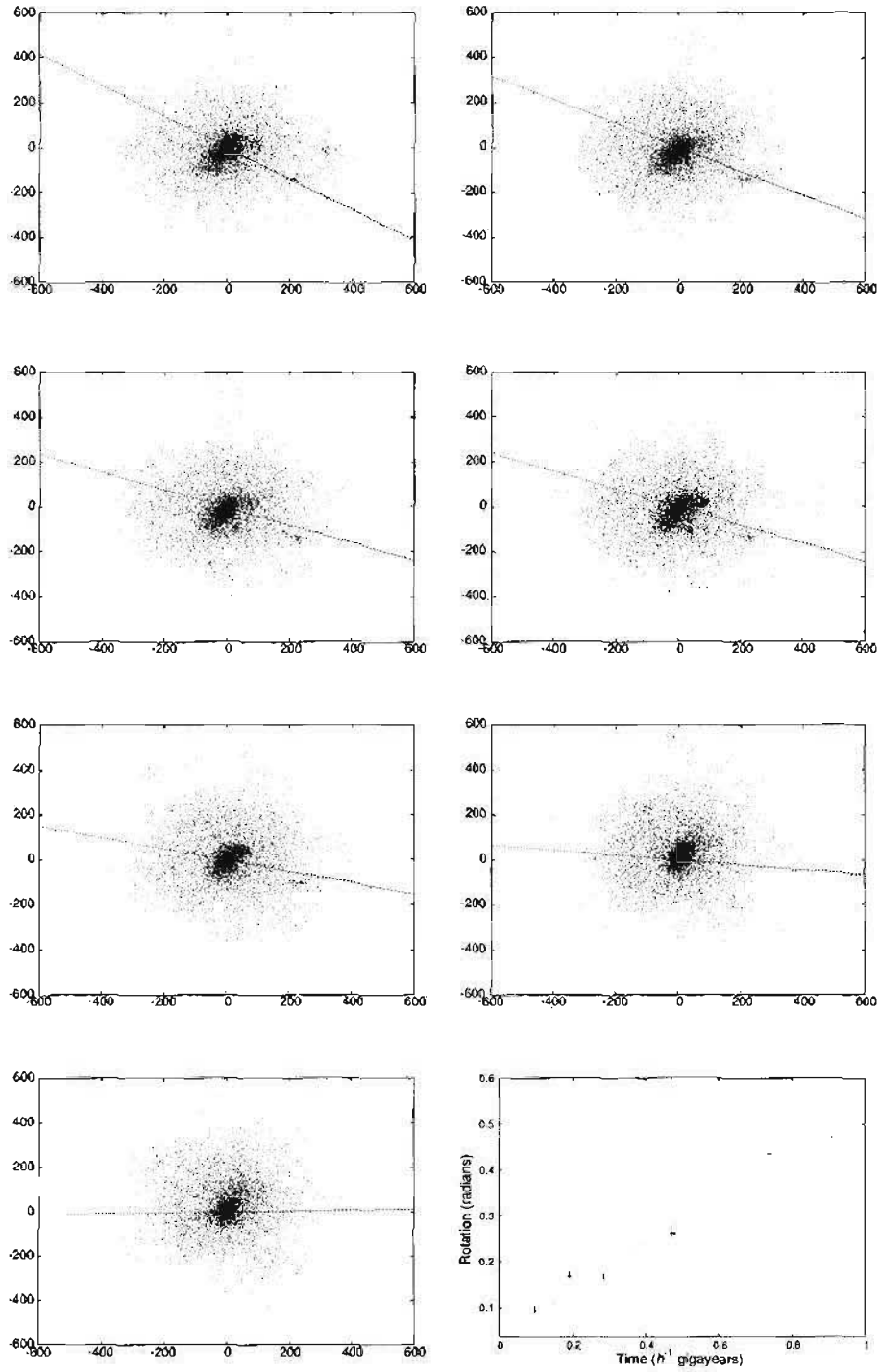
The first seven panels (left to right, top to bottom) show a projection of an undisturbed halo at redshifts 0, 0.01, 0.02, 0.03, 0.05, 0.08 and 0.1 (from top left) together with the halo's major axis. The vertical and horizontal axes give the distance from the centre of the halo in h^{-1} kpc. The bottom right figure shows the rotation of the major axis as a function of time.
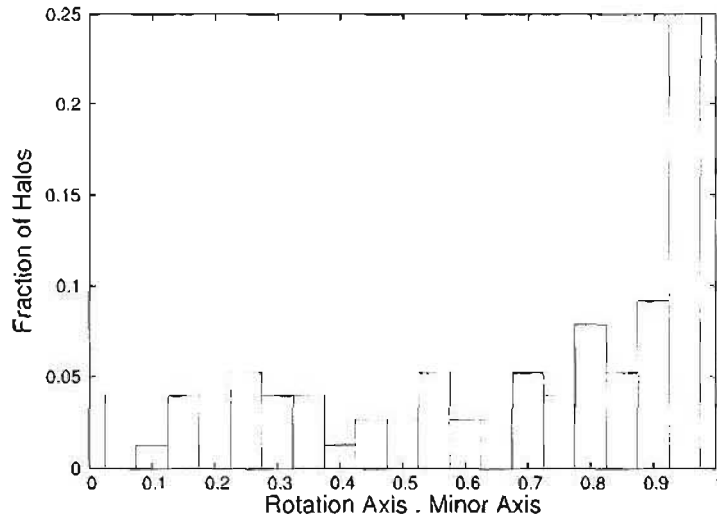
Figure 4.13: Alignment between Rotation Axis and Minor Axis

This figure shows the dot product between the rotation axis and the minor axis of the 76 halos in our sample. The rotation axis is fairly well aligned with the minor axis the halo.

Dubinski [1992], Pfitzner [1999] and Bailin and Steinmetz [2004] all noted that for the majority of their simulated halos the major axis appeared to rotate around the minor axis. To explore this, we have determined the dot product between the rotation axis and the minor axis of each of the halos in our sample. Figure 4.13 shows our results. We expect that the dot product between these axes will be close to one if they are well aligned. It appears that this is indeed the case for at least a third of our halos. We do, however, note that not all of our halos exhibit this alignment; this is probably due to the fact that we have considered the entire halo and not limited our calculation to a central spherical region of each halo in calculating the minor axis and rotation axis. While Bailin and Steinmetz [2004] found that at least 55 % of their rotating halos were aligned to within 25°, only 35 % of our halos show this alignment. If we consider only the spherical centre of the halos, the percentage of halos exhibiting this alignment increases to ~ 50%, agreeing with the results of Bailin and Steinmetz.

4.9 Pattern Speed

To determine the pattern speed of a halo, we have followed each halo over a period of about one gigayear. Figure 4.14 shows the rotation of the major axis as a function of time of one of the undisturbed halos selected from our sample; the other halos behave similarly (see appendix D). Using linear regression, we have found the best fit linear relation for the figure rotation of the halos as a function of time. The pattern speed of the halo is given by the slope of the linear fit. We have calculated the one sigma limit of the slope, and we have taken this to be the error in the pattern speed.

Figure 4.15 shows the pattern speeds obtained for this sample of 76 halos. The x-axis is the estimated error in pattern speeds. The green line represents the point at which the observed pattern speed is equal to the estimated error. We have also shown the point at which the pattern speed is equal to twice the estimated error (blue line). Halos with pattern speeds below the blue line would not be considered to be rotating coherently. Using this cutoff, 60% of the halos considered over a one gigayear period do, in fact, exhibit coherent rotation.

We found that the distribution of pattern speeds of the undisturbed halos from our simulation was well fit by the log normal distribution

$$P(\Omega_p) = \frac{1}{\Omega_p \, \sigma \, \sqrt{2\,\pi}} \, \exp\left(\frac{-\log^2\left(\frac{\Omega_p}{\mu}\right)}{2\,\sigma^2} \right) \, . \tag{4.5}$$

Figure 4.16 shows the distribution of pattern speeds for the halos considered, together with the log normal distribution (equation 4.5). Best fit values to this curve were found to be $\mu = -0.93 \pm 0.04$ and $\sigma = 0.40 \pm 0.04$. The mean pattern speed for this sample of halos is about $0.12h$ radians per gigayear ($6.9h$ degrees per gigayear). This is slightly slower than the mean pattern speed of $0.15h$ radians ($8.5h$ degrees) per gigayear obtained by Bailin and Steinmetz [2004] but our distribution (figure 4.16) agrees well with theirs. The fastest rotation that we have detected in our sample corresponds to a pattern speed of $0.93h$ radians per gigayear (about $53h$ degrees per gigayear).

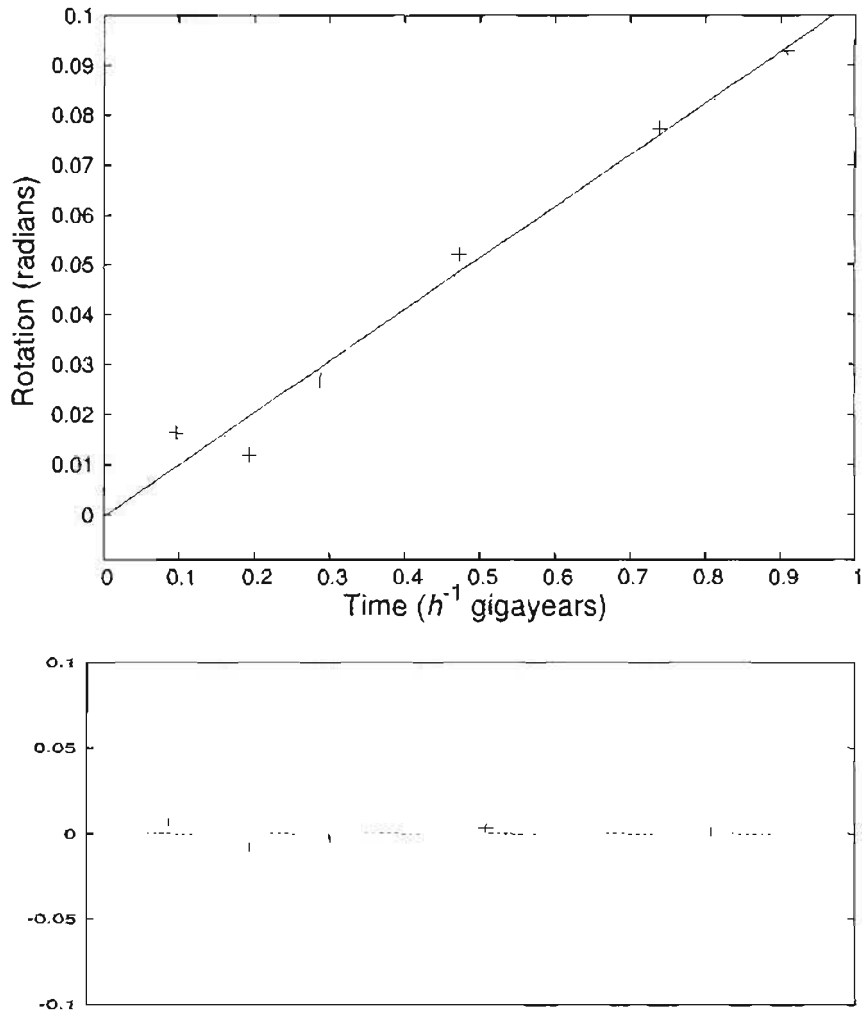Figure 4.14: Pattern Speed of a Single Halo Measured over One Gigayear
Top: The rotation of an undisturbed halo as a function of time over a one gigayear period. Each point represents the angle (in radians) that the halo has rotated over the time interval given. The slope of this plot (obtained by linear regression) gives the pattern speed of the halo.
Below: The residuals from the above fit.

54
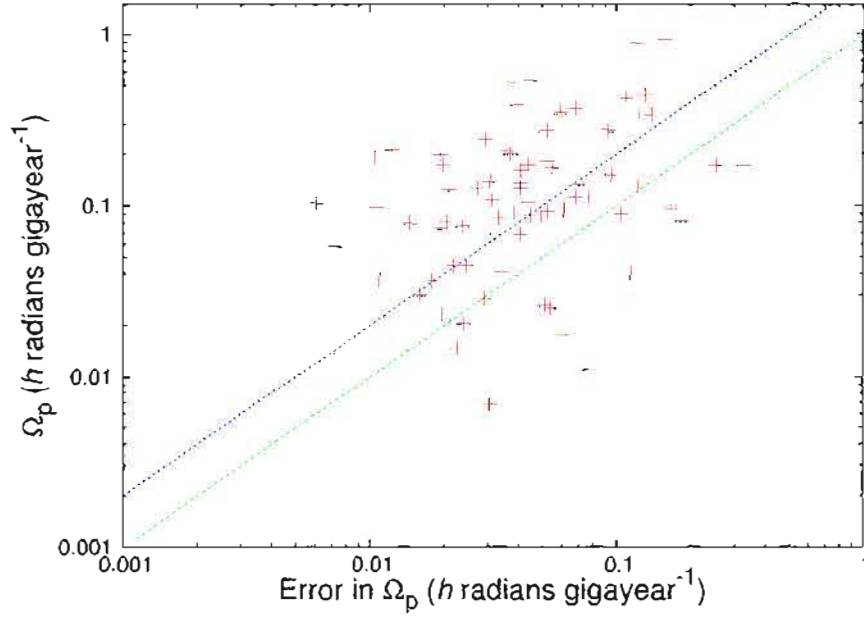
Figure 4.15: Uncertainties in Ω_p : Measurements for One Gigayear Period

This figure is a plot of the measured pattern speeds of the simulated halos versus the estimated error in pattern speed. The green line represents the point at which the pattern speed is equal to the estimated error (1 σ limit), the blue line depicts the point at which the pattern speed is equal to twice the error. Halos below the blue line, with pattern speeds less than twice the error, are not be considered to be rotating coherently.

Figure 4.16: Pattern Speed Distribution for a One Gigayear Period

This histogram shows the distribution of the pattern speeds calculated from the coherently rotating halos. The fit is a log normal distribution (equation 4.5) with $\mu = -0.93 \pm 0.04$ and $\sigma = 0.40 \pm 0.04$

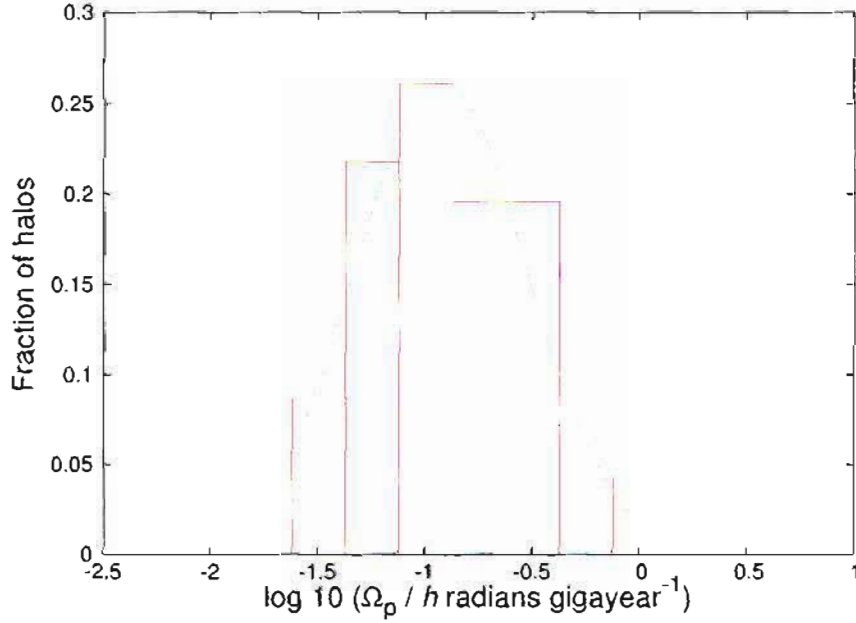We then considered the figure rotation over a longer period, of about three gigayears. The sample of halos considered for this period is smaller than that considered above, as more halos are affected by substructure at a higher redshift. We have found that from our simulation, 69 halos remain undisturbed over a three gigayear period.

Figure 4.17 shows the rotation of one of our halos that has remained unaffected by substructure over a three gigayear period; results are similar for the other halos (see appendix D). Figure 4.18 shows the pattern speeds of all of the 69 halos. As in figure 4.15 the x-axis is the estimated error in pattern speeds. The green line represents the point at which the observed pattern speed is equal to the estimated error. We have also shown the point at which the pattern speed is equal to twice the error (blue line). Recall that halos with pattern speeds less than twice the error are not considered to be rotating coherently.

We are now able to detect coherent rotation in 75% of the halos over this longer period. 29 of the 46 halos found to be rotating over a one gigayear period are also found to exhibit this rotation over the last three gigayears. We also identify 21 halos that were not considered to be rotating over one gigayear but are found to be rotating over this extended period.

As we have done for the rotation over one gigayear, we have plotted the distribution of pattern speeds observed over a period of three gigayears together with the log normal distribution given by equation 4.5 ($\mu = -1.04 \pm 0.01$ and $\sigma = 0.33 \pm 0.01$), shown in figure 4.19. The fastest rotation detected over this period was $0.41h$ radians per gigayear. The average pattern speed observed was $0.13h$ radians per gigayear. This is similar to the pattern speed measured over one gigayear period and agrees well with the average pattern speed found by Bailin and Steinmetz [2004]

Adjusting our cutoff, to include only those halos with pattern speeds greater than three times the error, does not significantly change the pattern speed distribution, best

56

fit values for this selection were $\mu = -1.03$ and $\sigma = 0.31$. The average pattern speed for the halos found to exhibit coherent rotation over both one and three gigayears (considering only halos with pattern speeds above three times the estimated error) was $0.14h$ radians per gigayear.

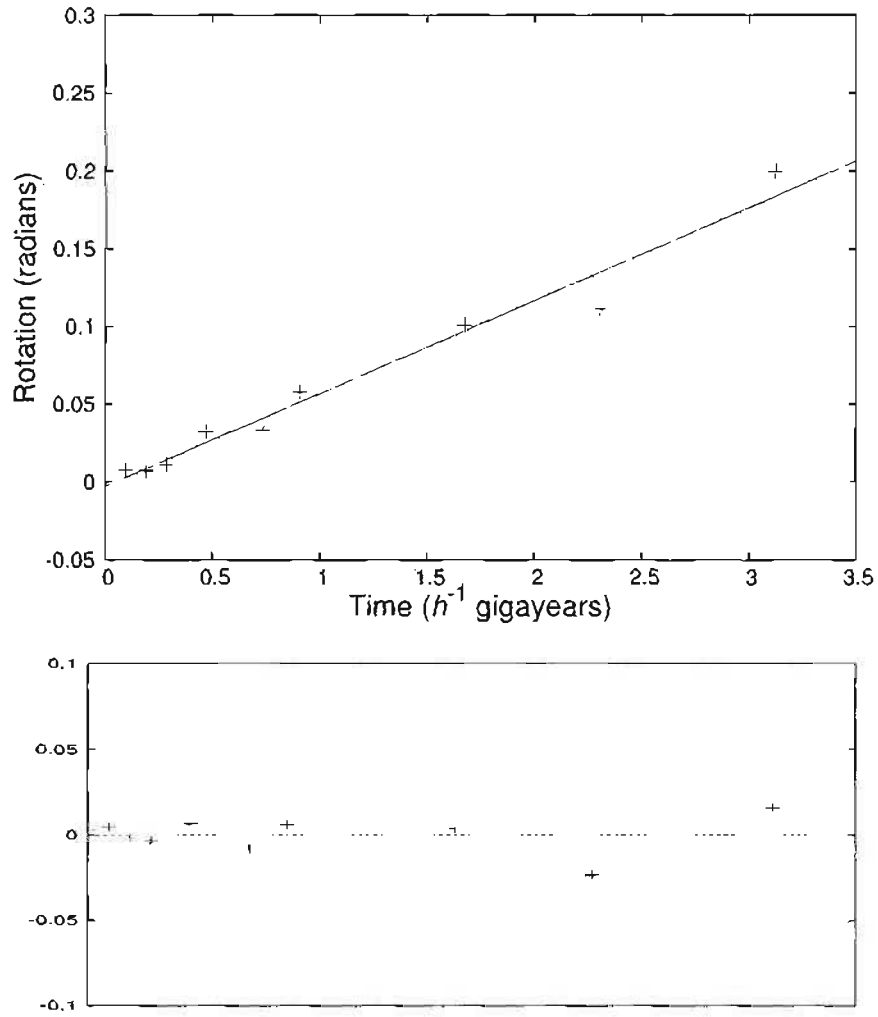Figure 4.17: Pattern Speed of a Single Halo Measured over Three Gigayears
Top: The rotation of an undisturbed halo as a function of time over a three gigayear period. Each point represents the angle (in radians) that the halo has rotated over the time interval given. The slope of this plot (obtained by linear regression) gives the pattern speed of the halo.
Below: The residuals from the above fit.
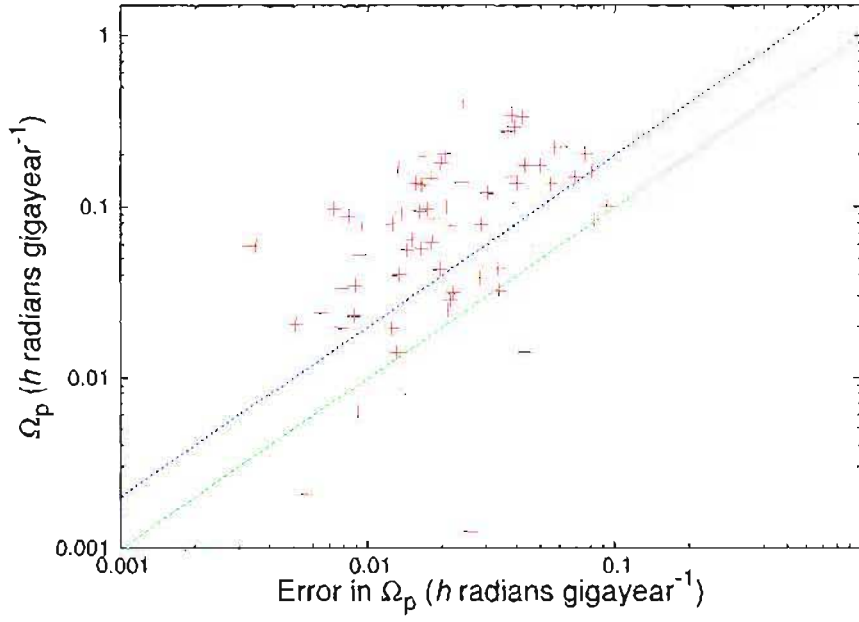
Figure 4.18: Uncertainties in Ω_p : Measurements for Three Gigayear Period

This figure is a plot of the measured pattern speeds of the simulated halos versus the estimated error in pattern speed. The green line represents the point at which the pattern speed is equal to the estimated error (1 σ limit), the blue line depicts the point at which the pattern speed is equal to twice the error. Halos below the blue line, with pattern speeds less than the twice the error are not considered to be rotating coherently.

Figure 4.19: Pattern Speed Distribution for a Three Gigayear Period

This histogram shows the distribution of the pattern speeds calculated from our undisturbed halos. The fit is a log normal distribution (equation 4.5) with $\mu = -1.04 \pm 0.01$ and $\sigma = 0.33 \pm 0.01$

4.10 Effect of Halo Properties on Pattern Speed
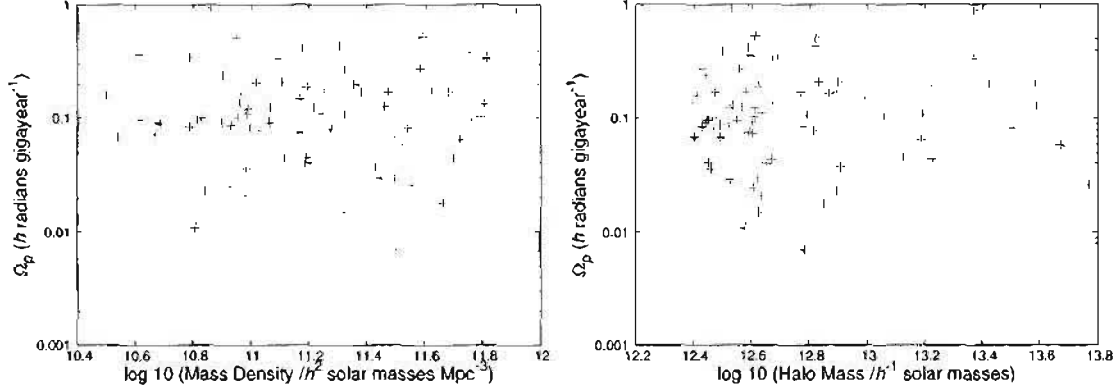
Figure 4.20: Pattern Speed versus Halo Properties
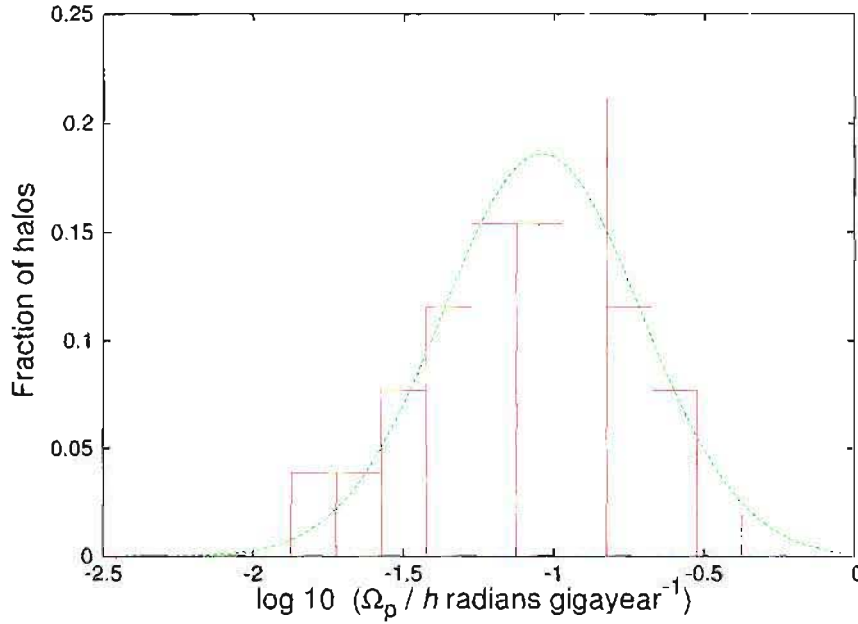The left plot is of pattern speed versus mass density in surrounding environment. The right plot shows pattern speed versus halo mass. There is no correlation between these halo properties and the observed pattern speed of the halo.

Finally, we have considered the effect of halo properties on the pattern speed. We have found no correlation between halo properties such as mass, or mass density in the surrounding environment and the observed pattern speed. To illustrate this we have, in figure 4.20, plotted a graph of halo pattern speed versus mass density and halo pattern speed versus halo mass. Clearly, the observed pattern speed is not dependent on either of these halo properties.

60

Chapter 5

Conclusions

We have simulated structure formation on cosmological scales using N-body simulations run on a single workstation, as well as in parallel on the University of KwaZulu-Natal's cluster of computers. We have simulated the evolution of 256^3 particles in a box of length $50\ h^{-1}$ Mpc using the parallel version of the publicly available GADGET code. We have used the results from these simulations to investigate aspects of galaxy formation and demonstrated that structure forms in a hierarchical manner in our simulated cold dark matter universe. In particular, our focus has been on the rotation of dark matter halos identified in these simulations.

We have found that the mass function determined from our simulation is well fit by the mass function obtained by Jenkins et al. [2001] using N-body simulations. This fit agrees well with the theoretical predictions of the Sheth and Tormen formula [Sheth and Tormen, 1999]. Our mass function also evolves with redshift as expected in a CDM universe.

We have calculated the dimensionless spin parameter for the halos identified in our simulations. The distribution of this spin parameter was found to be well fit by a log normal distribution (equation 4.4) with a best fit value of $\lambda_0' = 0.04$. This agrees well with the values found by Barnes and Efstathiou [1987] and Bullock et al. [2001].

Both of these tests suggest that the simulations we have run are reliable, agreeing with many previous simulations as well as with theoretical predictions.

From the halos identified in our simulations, we then eliminated all halos that had recently undergone a major merger from our sample as we are interested only in the motion of undisturbed halos. We have also eliminated all halos with significant substructure from our analysis. After eliminating the affected halos, we were left with a sample of 76 halos which were undisturbed over a period of one gigayear and a smaller sample of 69 halos unaffected over a three gigayear period.

We then considered the environment of the halos produced by our simulations. We have shown that the sample of undisturbed halos we have chosen for analysis tend to be in more dense environments than the average halos in the simulation. This is consistent with the results of Gottlöber et al. [2001] who suggest that the merger rate of isolated halos is higher than that of clusters and groups, at low redshifts ($z < 1$).

We found that 60% of the 76 halos considered over one gigayear did exhibit coherent rotation, and that the distribution of our pattern speeds was well fit by a log normal distribution centred at μ = -0.93 ± 0.04 (Ω_p = 0.12h radians per gigayear). The mean pattern speed detected in our sample is 0.12h radians per gigayear, while the highest pattern speed observed was 0.93h radians per gigayear. We have found that our halos exhibit pattern speeds of between 0.04 and 1.3 radians per gigayear (using h=0.7) when determined over a one gigayear period. The pattern speeds of our selected halos, determined over a one gigayear period, compare favourably with those found by Dubinski [1992], who found that his halos were rotating with pattern speeds between 0.1 and 1.6 radians per gigayear. The pattern speed of 1.1 radians per gigayear detected by Pfitzner [1999] is also consistent with the pattern speeds found in our simulation over this period. The mean pattern speed of our simulated halos, measured over one gigayear, is 0.12h radians per gigayear, this compares favourably to the mean of 0.15h radians per gigayear found by Bailin and Steinmetz [2004]. The

difference is probably due to the fact that we have considered the entire halo and not restricted our analysis to the central region of the halos.

Of the smaller sample of halos, undisturbed over a three gigayear period, 75% were found to rotate coherently. Again, the distribution was well fit by a log normal curve. Best fit values of μ and σ were, for this period, -1.04 $\pm$ 0.01 (Ω_p = 0.09h radians per gigayear) and 0.33 $\pm$ 0.01 respectively. The highest pattern speed detected over this period was 0.41h radians per gigayear. The average pattern speed over a three gigayear period was 0.13h radians per gigayear, consistent with the value determined over a one gigayear period.

Our pattern speeds are significantly smaller than the speeds believed to be required to produce spiral structure (as suggested by Bureau et al. [1999]).

In this project we have shown that many of the undisturbed halos selected from our cold dark matter simulation do exhibit coherent rotation over a period of three gigayears. This places serious doubt on the validity of the assumption of stationary dark matter halos.

In studying the relationship between the figure rotation axis and the minor axis, we found alignment for many of the halos but a significant fraction which were not very well aligned. The two axes are within 25° of each other in 35% of the halos, using our definition of a halo. If we restricted our analysis to the central region as did Bailin and Steinmetz [2004], our results agree with theirs.

We have found no correlation between halo properties such as halo mass, or environment and the pattern speed.

With GADGET now setup and running in parallel on the KwaZulu-Natal cluster, many projects can be undertaken. To extend the work done in this project it would be

interesting to explore the characteristics of the galaxies embedded in these dark halos. This could be done by including semi-analytical modelling which would allow us to say how much light is in the spheroidal and disk components of the galaxies, and would, therefore, allow us to identify halos associated with specific galaxy types. It would also be interesting to study the effects of major mergers on the dark matter halos. As more processors are added to the cluster, we will be able to increase the number of particles simulated, and thereby increase the resolution of future simulations.

Bibliography

Athanassoula, E., Fady, E., Lambert, J. C., and Bosma, A. (2000). Optimal Softening for Force Calculations in Collisionless N-body Simulations. *Mon. Not. R. Astron. Soc.*, 314:475–488.

Bailin, J. and Steinmetz, M. (2004). Figure Rotation of Cosmological Dark Matter Halos. *The Astrophysical Journal*, 616:27–39.

Bardeen, J., Bond, J., Kaiser, N., and Szalay, A. (1986). The Statistics of Peaks of Gaussian Random Fields. *The Astrophysical Journal*, 304:15–61.

Barnes, J. and Efstathiou, G. (1987). Angular Momentum from Tidal Torques. *The Astrophysical Journal*, 319:575–600.

Bekki, K. and Freeman, K. (2002). Extended HI Spiral Structure and the Figure Rotation of Triaxial Dark Halos. *The Astrophysical Journal*, 574:L21–L24.

Bullock, J., Dekel, A., Kolatt, T., Kravtsov, A., Klypin, A., Porciani, C., and Primack, J. (2001). A Universal Angular Momentum Profile for Galactic Halos. *The Astrophysical Journal*, 555:240–257.

Bureau, M., Freeman, K., Pfitzner, D., and Meurer, G. (1999). The Shape and Figure Rotation of the Dark Halo NGC 2915. *The Astronomical Journal*, 118:2158–2171.

Davis, M., Efstathiou, G., Frenk, C., and White, S. (1985). The Evolution of Large Scale Structure in a Universe Dominated by Cold Dark Matter. *The Astrophysical Journal*, 292:371–394.

de Blok, W. J. G., McGaugh, S. S., Bosma, A., and Rubin, V. C. (2001). Mass Density Profiles of Low Surface Brightness Galaxies. *The Astrophysical Journal*, 69:103–501.

De Lucia, G., Kauffmann, G., Springel, V., White, S., Lanzoni, B., Stoehr, F., Tormen, G., and Yoshida, N. (2003). Substructures in Cold Dark Matter Haloes. *Mon. Not. R. Astron. Soc*, 348:333–344.

de Zeeuw, T. and Franx, M. (1991). Structure and Dynamics of Elliptical Galaxies. *Annual Review of Astronomy and Astrophysics*, 29:239–274.

Dubinski, J. (1992). Cosmological Tidal Shear. *The Astrophysical Journal*, 401:441–454.

Dubinski, J. (1996). A Parallel Tree Code. *New Astronomy*, 1:133–147.

Dubinski, J. and Carlberg, R. (1991). The Structure of Cold Dark Matter Halos. *The Astrophysical Journal*, 378:496–503.

Efstathiou, G., Davis, M., Frenk, C., and White, S. (1985). Numerical Techniques for Large Cosmological N-Body Simulations. *The Astrophysical Journal*, 57:241–260.

Efstathiou, G. and Eastwood, J. W. (1981). On the Clustering of Particles in an Expanding Universe. *Mon. Not. R. Astron. Soc.*, 194:503–525.

Goldstein, H. (1980). *Classical Mechanics Second Edition*. Addison-Wesley Publishing Company.

Gottlöber, S., Klypin, A., and Kravtsov, A. V. (2001). Merging History as a Function of Halo Environment. *The Astrophysical Journal*, 546:223–233.

Gunn, J. E. (1980). The Dynamics of Galaxies and the 'Missing Mass' Problem. *Royal Society of London Philosophical Transactions Series A*, 296:313–318.

Hernquist, L., Bouchet, F. R., and Suto, Y. (1990). Application of the Ewald Method to Cosmological N-Body Simulations. *The Astrophysical Journal*, 75:231–240.

Jenkins, A., Frenk, C., White, S., Colberg, J., Cole, S., Evrard, A., Couchman, H., and Yoshida, N. (2001). The Mass Function of Dark Matter Haloes. *Mon. Not. R. Astron. Soc.*, 321:372–384.

Jones, M. H. and Lambourne, R. J. A. (1993). *An Introduction to Galaxies and Cosmology*. Cambridge University Press, Cambridge, United Kingdom.

Kauffmann, G. and White, S. (1993). The Merging History of Dark Matter Haloes in a Hierarchical Universe. *Mon. Not. R. Astron. Soc.*, 261:921–928.

Kolb, E. and Turner, M. S. (1993). *The Early Universe*. Addison-Wesley Publishing Company.

Lemson, G. and Kauffmann, G. (1999). Environmental Influences on Dark Matter Haloes and Consequences for the Galaxies within them. *Mon. Not. R. Astron. Soc*, 302:111–117.

Ma, C. and Bertschinger, E. (1995). Cosmological Perturbation Theory in the Synchronous and Conformal Newtonian Gauges. *The Astrophysical Journal*, 455:7–25.

Masset, F. and Bureau, M. (2003). On the Spiral Structure of NGC 2915 and Dark Matter. *The Astrophysical Journal*, 586:152–169.

Merritt, D. (1996). Optimal Smoothing for N-body Codes. *The Astronomical Journal*, 111:2462–2464.

Peebles, P. (1969). Origin of the Angular Momentum of Galaxies. *The Astrophysical Journal*, 155:393–401.

Pfitzner, D. (1999). PhD thesis, Australian National University.

Porciani, C., Dekel, A., and Hoffman, Y. (2002a). Testing Tidal-Torque Theory: I. Spin Amplitude and Direction. *Mon. Not. R. Astron. Soc*, 332:325–338.

Porciani, C., Dekel, A., and Hoffman, Y. (2002b). Testing Tidal-Torque Theory: II. Alignment of Inertia Shear and the Characteristics of Proto-haloes. *Mon. Not. R. Astron. Soc*, 332:339–351.

Power, C., Navarro, J. F., Jenkins, A., Frenk, C. S., White, S. D. M., Springel, V., Stadel, J., and Quinn, T. (2003). The Inner Structure of ΛCDM Haloes - I. A Numerical Convergence Study. *Mon. Not. R. Astron. Soc.*, 338:14–34.

Press, W., Teukolsky, S., Vetterling, W., and Flannery, B. (1992). *Numerical Recipes in Fortran*. Cambridge University Press.

Reed, D., Gardner, J., Quinn, T., Stadel, T., Fardal, M., and Lake, G. (2003). Evolution of the Mass Function of Dark Matter Haloes. *Mon. Not. R. Astron. Soc*, 346:565–572.

Sheth, R. and Tormen, G. (1999). Large-scale Bias and the Peak Background Split. *Mon. Not. R. Astron. Soc*, 308:119–126.

Shreiner, D., Woo, M., Neider, J., and Davis, T. (2004). *OpenGL Programming Guide Fourth Edition*. Addison-Wesley Publishing Company.

Spergel, D. N., Verde, L., Peiris, H. V., Komatsu, E., Nolta, M. R., Bennett, C. L., Halpern, M., Hinshaw, G., Jarosik, N., Kogut, A., Limon, M., Meyer, S. S., Page, L., Tucker, G. S., Weiland, J. L., Wollack, E., and Wright, E. L. (2003). First-Year Wilkinson Microwave Anisotropy Probe (WMAP) Observations: Determination of Cosmological Parameters. *The Astrophysical Journal*, 148:175–194.

Springel, V., White, S. D. M., Jenkins, A., Frenk, C. S., Yoshida, N., Gao, L., Navarro, J., Thacker, R., Croton, D., Helly, J., Peacock, J. A., Cole, S., Thomas, P., Couchman, H., Evrard, A., Colberg, J., and Pearce, F. (2005). Simulations of the Formation, Evolution and Clustering of Galaxies and Quasars. *Nature*, 435:629–636.

Springel, V., Yoshida, N., and White, S. D. M. (2001). GADGET: A Code for Collisionless and Gasdynamical Cosmological Simulations. *New Astronomy*, 6:79–117.

Sugerman, B., Summers, F., and Kamionkowski, M. (2000). Testing Linear-Theory Predictions of Galaxy Formation. *Mon. Not. R. Astron. Soc*, 311:762–780.

Tegmark, M., Strauss, M. A., Blanton, M. R., Abazajian, K., Dodelson, S., Sandvik, H., Wang, X., Weinberg, D. H., Zehavi, I., Bahcall, N. A., and co authors, . (2004). Cosmological Parameters from SDSS and WMAP. *Physical Review D*, 69:103–501.

van de Weygaert, R. and Bertschinger, E. (1996). Peak and Gravity Constraints in Gaussian Primordial Density Fields: and Application of the Hoffman-Ribak Method. *Mon. Not. R. Astron. Soc.*, 281:84–118.

Warren, M., Quinn, P., Salmon, J., and Zurek, W. (1992). Dark Halos formed via Dissipationless Collapse. I. Shapes and Alignment of Angular Momentum. *The Astrophysical Journal*, 399:405–425.

Appendix A

Visualisation using Open GL

Open GL (Graphics Library) is an open source software interface to graphics hardware which allows visualisation of problems relatively simply. Developed by Silicon Graphics, it has become a standard graphics library consisting of about 250 commands which can be used on many different hardware platforms. Open GL is a low level language and a model is built using simple geometric primitives such as points and lines.

We have used Open GL to visualise a small simulation. This program allows us to step through time, observing the formation of structure in our simulation. Figure A.1 shows three screen shots taken from our Open GL program; these have been taken at different time steps and clearly show the particles falling together under gravity.

The advantage to using Open GL is that the model is interactive - the user is able to zoom in and out, rotate the box through any angle in the x,y or z direction and to step through time as desired. To illustrate this we have included screen shots of our model from different angles in figure A.2
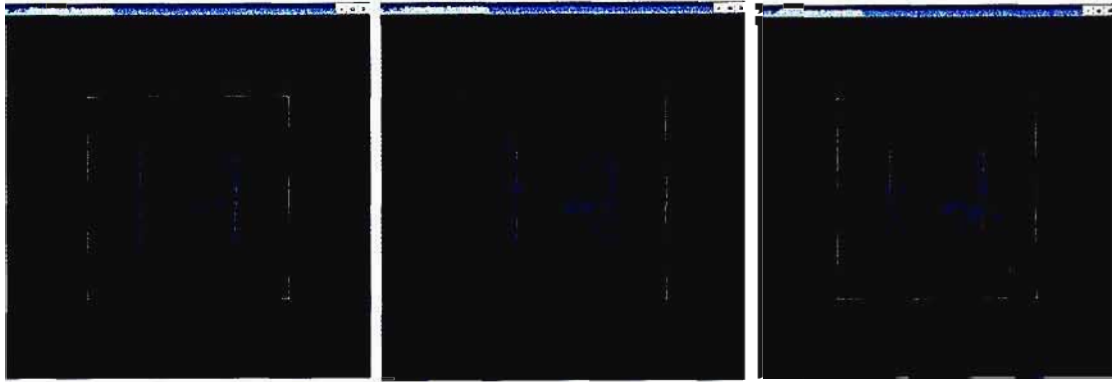
Figure A.1: Evolution of Structure in Simulated Box

These three screen shots show the simulated box at different timesteps. Time is increasing to the right.
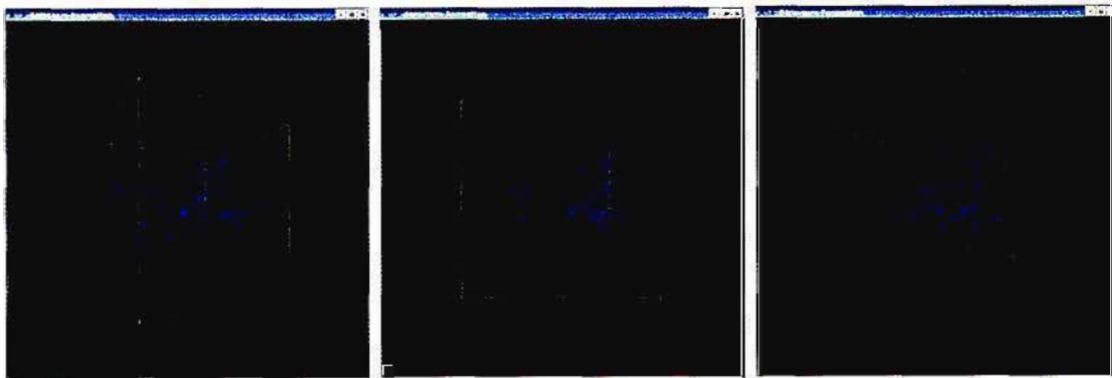

Figure A.2: Rotation of Simulated Box

The three screen shots above, show the simulated box from different angles.

Appendix B

Linear Structure Formation

The Cosmic Microwave background provides evidence that the universe was initially very smooth. Yet today, on small scales, we see an abundance of substructure. In fact, at the time of decoupling

$$\left(\frac{\delta\rho}{\rho}\right)_{\text{dec}} = \text{const} \times \left(\frac{\delta T}{T}\right) \lesssim \mathcal{O}(10^{-2} - 10^{-3}) \tag{B.1}$$

while today the density of galaxies is about 10^5 times the average density of the universe and the density of galaxy clusters is $\sim 10^3$ times this average density.

How does structure form out of such smooth initial conditions?
It is often assumed that the density fluctuations in the universe result from quantum fluctuations greatly amplified during an inflationary phase.
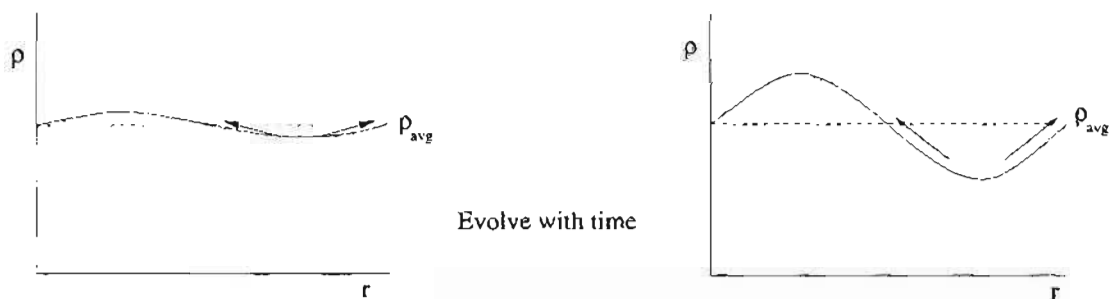
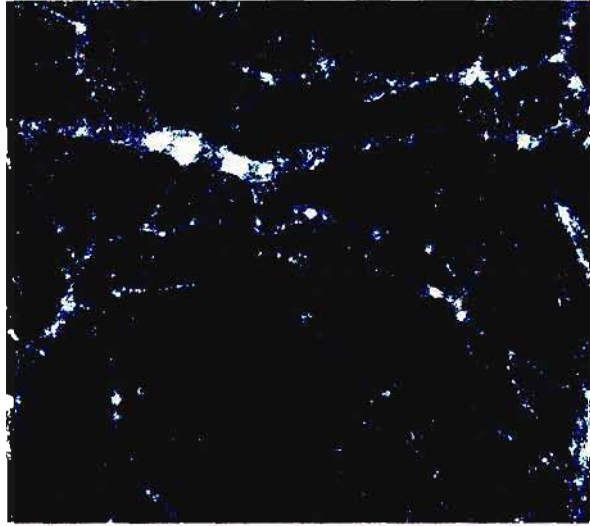Origin of structure: the growth of density fluctuations.

Figure B.1: Simulated Large-Scale Structure
Initial fluctuations collapse under their own gravity to produce large-scale structure.
This is a FITS image of a projected slice of the simulated box at redshift zero, showing filaments
(particularly over dense regions) and voids (under dense regions).

Initially, the overdensities will expand with the background expansion, the expansion of these overdensities will progress at a slower rate than the background expansion and the overdensitites will eventually break away from the expansion to collapse under their own gravity and form virialised systems.

As a starting point for understanding the formation of structure we will consider how we expect matter in general to cluster within the linear regime. We will then apply this to dark matter in the linear regime. In order to go beyond this, into the non-linear regime, we use the simulations discussed in the main part of the thesis..

B.1 Newtonian Structure Formation

The universe is expanding, constantly changing with time; because of this it is useful to express fluctuations in density as a density contrast.

Fractional Density Contrast is defined as

$$\delta\left(\mathbf{x}\right) \equiv \frac{\delta\,\rho\left(\mathbf{x}\right)}{\bar{\rho}} = \frac{\rho\left(\mathbf{x}\right) - \bar{\rho}}{\bar{\rho}}\,. \tag{B.2}$$

Density is then given by

$$\rho(\mathbf{r},t) = \bar{\rho}(t)\left[1 + \delta(\mathbf{r},t)\right]\,. \tag{B.3}$$

The Growth of an Overdensity

Consider a spherical region of space. The mass contained within that sphere is given by

$$M = \rho V = \bar{\rho}(t)\left[1 + \delta(\mathbf{r},t)\right] \times \frac{4}{3}\pi R^3\,. \tag{B.4}$$

Conservation of mass requires this (equation B.4) to be constant.

From this we can see that $R \propto \frac{\bar{\rho}(t)^{-\frac{1}{3}}}{[1+\delta(t)]^{\frac{1}{3}}}$ and, knowing that for matter $\rho_m \propto a^{-3}$, we have

$$R \propto \frac{a(t)}{[1 + \delta(t)]^{\frac{1}{3}}}\,. \tag{B.5}$$

This means that for positive fluctuations ($\delta > 0$) the radius $R(t)$ must grow at a slower rate than the scale factor a. When this is the case, the sphere will break away from the expansion and collapse. The time at which $R(t)$ stops growing is known as turnaround time.
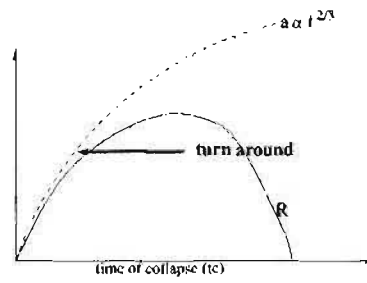
The Evolution of Density Fluctuations $\delta(t)$

As a first step, we will neglect general relativity and use a classical Newtonian approach. This is sufficient provided the size of the structure is much smaller than the horizon distance ($l \ll d_H$). We will follow the approach given by Kolb and Turner [1993]

B.2 Perturbation Growth in a Non-Expanding Fluid

If we define ρ to be the matter density, $\mathbf{v}$ to be the local fluid velocity, p to be the matter pressure and ϕ to be the gravitational potential then we can state the perfect fluid equations as follows

$$\frac{\partial \rho}{\partial t} + \nabla \cdot (\rho \, \mathbf{v}) = 0$$

$$\frac{\partial \mathbf{v}}{\partial t} + (\mathbf{v} \cdot \nabla)\mathbf{v} + \frac{1}{\rho} + \nabla p + \nabla \phi = 0 \qquad (B.6)$$

$$\nabla^2 \phi = 4\pi G \rho \,.$$

The equations in B.6 are known as the Continuity equation, Euler equation and Poisson equation respectively.

The simplest solution to the fluid equations would be one in which the matter is both evenly distributed and stationary - a static state. That is, the density and pressure are constant, and the velocity is zero. We also assume that the gravitational potential in such a state is zero, that is $\nabla \phi_0 = 0$. This step is known as the 'Jeans swindle'. ($\rho_0 = $ constant, $p_0 = $ constant, $\mathbf{v}_0 = 0$). Note that we have used the subscript 0 to denote an unperturbed quantity. If we now consider a small perturbation about this static (unperturbed) state, we can express the density in the perturbed state as the sum of the density in the unperturbed state and the density contribution of the perturbation, i.e. $\rho = \rho_0 + \rho_1$. The subscript 1 will be used to represent a small perturbation from the static state. The increase in density at a point in the region will give rise to a pressure $p = p_0 + p_1$, a velocity, $\mathbf{v} = \mathbf{v}_0 + \mathbf{v}_1$ and a potential $\phi = \phi_0 + \phi_1$. We can then describe the perturbed state by the following

$$\rho = \rho_0 + \rho_1$$

$$p = p_0 + p_1$$

$$\mathbf{v} = \mathbf{v_0} + \mathbf{v_1}$$

$$\phi = \phi_0 + \phi_1 \,.$$

(B.7)

We will consider adiabatic perturbations; this means that the equation of state (relating pressure to density) $P = P(\rho)$, is independent of spatial coordinates. The sound speed (v_s^2) is defined as the rate of change in pressure with respect to density, but since we are considering only adiabatic perturbations, we can write this as

$$v_s^2 \equiv \left(\frac{\partial p}{\partial \rho}\right) = \frac{p_1}{\rho_1} \,.$$

(B.8)

Substituting the perturbed quantities (density, pressure, velocity and potential) as given in equation B.7 into the

- *Continuity Equation* we get $\frac{\partial \rho_1}{\partial t} + \rho_0 \nabla \cdot \mathbf{v_1} = 0$. Since $\mathbf{v_0} = 0$ and $\rho = $ constant. Here we have neglected higher order terms such as $(\rho_1 (\nabla \cdot \mathbf{v_1}))$

- *Euler Equation* gives $\frac{\partial \mathbf{v}}{\partial t} + \frac{v_s^2}{\rho_0} \nabla \rho_1 + \nabla \phi_1 = 0$. Since, as the perturbations are very small, the velocities will be very small. This makes the term $(\mathbf{v} \cdot \nabla)\mathbf{v}$ zero. Also, since the perturbations are so small, $\rho_1 \ll \rho_1$ and $\frac{1}{\rho_0 + \rho_1} \approx \frac{1}{\rho_0}$

- *Poisson Equation* yields $\nabla^2 \phi_1 = 4\pi G \rho_1$. An unperturbed region, where matter is uniformly distributed, will not experience a potential. The potential is due to the perturbation only.

The perturbed versions of the perfect fluid equations are then, to a first order approximation, given by

76

$$\frac{\partial \rho_1}{\partial t} + \rho_0 \nabla \cdot \mathbf{v}_1 = 0$$

$$\frac{\partial \mathbf{v}}{\partial t} + \frac{v_s^2}{\rho_0} \nabla \rho_1 + \nabla \phi_1 = 0 \qquad \text{(B.9)}$$

$$\nabla^2 \phi_1 = 4 \pi G \rho_1 \, .$$

It is possible to combine the three equations from B.9. This is done by taking $\frac{d}{dt}$ of the perturbed continuity equation and substituting into this the perturbed version of the Euler and Poisson equations. Doing so results in a second order differential equation for ρ_1,

$$\frac{\partial^2 \rho_1}{\partial t^2} - v_s^2 \nabla^2 \rho_1 = 4 G \rho_0 \rho_1 \, , \qquad \text{(B.10)}$$

which has the solutions of the form

$$\rho_1(\mathbf{r}, t) = \delta(\mathbf{r}, t) \rho_0 = A \exp\left(- i \, \mathbf{k} \cdot \mathbf{r} + i \omega \, t\right) \rho_0 \qquad \text{(B.11)}$$

and ω and $\mathbf{k}$ satisfy the dispersion relation

$$\omega^2 = v_s^2 k^2 - 4\pi G \rho_0 \, . \qquad \text{(B.12)}$$

The type of solutions found depend on whether ω is imaginary or real.

If ω is imaginary, that is if $v_s^2 \, k^2 < 4 \pi G \rho$, the solutions correspond to exponentially growing modes.

However, when ω is real, $v_s^2 \, k^2 > 4 \pi G \rho$, the solutions are of a sinusoidal nature.

The perturbations will oscillate as sound waves. For ω to be real, the sound speed must be the dominant term; this means that there must be significant pressure (recall the definition of sound speed equation B.8). This pressure acts against the gravitational collapse, causing oscillations.

Clearly, there must be some critical value separating these behaviours. Using equation B.12 we can define that critical value to be

$$k_J = \left(\frac{4\pi G \rho}{v_s^2} \right) .$$
(B.13)

where any values of $k < k_J$ will result in exponential growth (collapse), and values of $k > k_J$ will create oscillations. k_J is known as the Jeans wavenumber.

It is also useful to define the Jeans Length λ_J and the Jeans Mass M_J

$$\lambda = 2\frac{\pi}{k_J}$$
$$M_J \equiv \frac{4\pi}{3} \left(\frac{\pi}{k_J} \right)^3 = \frac{\pi^{\frac{5}{2}}}{6} \frac{v_s^3}{G^{\frac{3}{2}} \rho_0^{\frac{1}{2}}} .$$
(B.14)

The Jeans mass is simply the total mass contained within a sphere of radius $\frac{\lambda_J}{2}$. Masses less than M_J are stable, whereas masses greater than M_J are not and will undergo collapse.

The timescale of the gravitational collapse is known as Dynamical timescale and is given by

$$\tau_{\text{dyn}} = (\text{Im}\omega)^{-1} \approx (4\pi G\rho_0)^{\frac{-1}{2}} .$$
(B.15)

For pressure to act at any given length, enough time must have elapsed; this sets the timescale for a 'pressure response' to be

$$\tau_{\text{pressure}} \sim \frac{\lambda}{v_s} .$$
(B.16)

If $\tau_{\text{dynamic}} > \tau_{\text{pressure}}$ the collapse will occur before the pressure is able to stabilise the system, and restore hydrostatic equilibrium. $\tau_{\text{dynamic}} > \tau_{\text{pressure}}$ when $\lambda \gtrsim \frac{v_s}{(G\rho_0)^{\frac{1}{2}}} \sim \lambda_J$. This sets a length scale which will be stable to gravitational collapse.

B.3 Growth of Perturbations in an Expanding Fluid

Our discussion so far has ignored the expansion of the universe. For a thorough understanding of the linear nature of structure formation we must consider the effects of this expansion.

Firstly, when considering the expansion of the universe the unperturbed quantities of density, velocity and potential are given by

$$
\begin{aligned}
\rho_0 &= \rho_0(t_0)\, a^{-3}(t) \\
\mathbf{v} &= \tfrac{\dot{a}}{a}\, \mathbf{r} \\
\nabla \phi_0 &= \tfrac{4\pi G \rho_0}{3}\, \mathbf{r}\,.
\end{aligned}
\tag{B.17}
$$

These perturbations then satisfy the following hydrodynamical equations

$$
\begin{aligned}
\frac{\partial \rho_1}{\partial t} + 3\frac{\dot{a}}{a}\rho_1 + \frac{\dot{a}}{a}(\mathbf{r}\cdot\nabla)\,\rho_1 + \rho_0\nabla\cdot\mathbf{v}_1 &= 0 \\
\frac{\partial \mathbf{v}_1}{\partial t} + \frac{\dot{a}}{a}\mathbf{v}_1 + \frac{\dot{a}}{a}(\mathbf{r}\cdot\nabla)\,\mathbf{v}_1 + \frac{v_s^2}{\rho_0}\nabla\phi_1 &= 0 \\
\nabla^2\phi_1 &= 4\pi G \rho_1\,.
\end{aligned}
\tag{B.18}
$$

In order to simplify this problem considerably we define $\delta(\mathbf{r}, t) = \frac{\rho_1}{\rho_0}$ and use a Fourier Expansion of the form

$$
\psi(\mathbf{r}, t) = (2\pi)^{-3} \int \psi_k(t) exp\left[\frac{-i\,\mathbf{k}\cdot\mathbf{r}}{a(t)}\right] d^3r
\tag{B.19}
$$

for the perturbations in density, velocity and potential of the system ($\psi = \rho_1, \mathbf{v}_1, \phi_1$). In doing this, the equations B.18 become

$$
\begin{aligned}
\dot{\delta}_k - \frac{i\mathbf{k}}{a}\cdot\mathbf{v}_k &= 0 \\
\frac{d(a\,\mathbf{v}_k)}{dt} - ikv_s^2\delta_k - ik\phi_k &= 0 \\
\phi_k &= -\frac{4\pi G \rho_0}{k^2}a^2\delta_k\,.
\end{aligned}
\tag{B.20}
$$

It is also useful to split the velocity into rotational ($\mathbf{v}_\perp$) and irrotational ($\mathbf{v}_\parallel$) components.

Then $\mathbf{v}_k$ can be expressed as

$$\mathbf{v}_k = \mathbf{v}_\parallel(\mathbf{k}) + \mathbf{v}_\perp(\mathbf{k}) \, . \tag{B.21}$$

Also, we know that

$$
\begin{aligned}
&\nabla \cdot \mathbf{v}_\perp = 0 \\
&\nabla \times \mathbf{v}_\parallel = 0 \\
&\mathbf{k} \cdot \mathbf{v}_\perp(\mathbf{k}) = 0 \\
&\mathbf{k} \cdot \mathbf{v}_\parallel(\mathbf{k}) = \|\mathbf{k}\| \, \|\mathbf{v}_\parallel(\mathbf{k})\| \, .
\end{aligned}
\tag{B.22}
$$

Thus the perturbed equations B.18 can be written (to a first order approximation) as

$$
\begin{aligned}
&\frac{d(a\,\mathbf{v}_\perp(\mathbf{k}))}{dt} = 0 \Rightarrow \mathbf{v}_\perp \propto a(t)^{-1} \\
&\mathbf{v}_\parallel(\mathbf{k}) = \frac{a}{ik}\,\dot{\delta}_k + \frac{\text{const}}{a(t)} \\
&\ddot{\delta}_k + 2\frac{\dot{a}}{a}\dot{\delta}_k + \left(\frac{v_s^2 k^2}{a^2} - 4\pi G \rho_0\right)\delta_k = 0 \, .
\end{aligned}
\tag{B.23}
$$

We will focus our attention on the last of these

$$\ddot{\delta} + 2\frac{\dot{a}}{a}\dot{\delta} + \left[\frac{v_{si}^2\,k^2}{a^2}\,\delta_i - 4\pi G\,\rho_0 \sum_j c_j\,\delta_j\right] = 0 \, . \tag{B.24}$$

Since we are only interested in dark matter the term $\frac{v_{si}^2\,k^2}{a^2}$ is zero, as there is no pressure. And we can rewrite equation B.24 as

$$\ddot{\delta} + 2\frac{\dot{a}}{a}\dot{\delta} + 4\pi G\,\rho_0\,\delta = 0 \, . \tag{B.25}$$

In order to proceed we need to say something about $\frac{\dot{a}}{a}$. We will do this firstly for a static universe and then for an expanding universe.

81

- **A Static universe**

  For a static universe $H = \frac{\dot{a}}{a} = 0$, then from equation B.25 we have $\ddot{\delta} \propto \delta$. This means that in a static universe dark matter would experience exponential growth, as was the case with the non expanding fluid.

  $$\delta \propto e^{\frac{t}{t_c}} , \tag{B.26}$$

  Expansion in a static universe is too fast to explain the structures we observe today.

- **An expanding universe**

  In an expanding universe $H = \frac{\dot{a}}{a} \neq 0$ and we no longer have exponential growth. The non-zero H acts as a friction term slowing the perturbation growth. The Friedmann equation is given by

  $$H^2 = \left(\frac{\dot{a}}{a}\right)^2 = \frac{8\pi G \rho}{3} - \frac{k^3}{a} + \frac{\Lambda}{3} . \tag{B.27}$$

  From this we can define a critical density, ρ_c as

  $$\rho_c = \frac{3H^2}{8\pi G} . \tag{B.28}$$

  Using this definition of critical density and the fact that $\frac{\bar{\rho}_m}{\rho_c} = \Omega_m$, we can re-write the Friedmann equation (with no curvature (k=0) and no cosmological constant ($\Lambda = 0$)) as

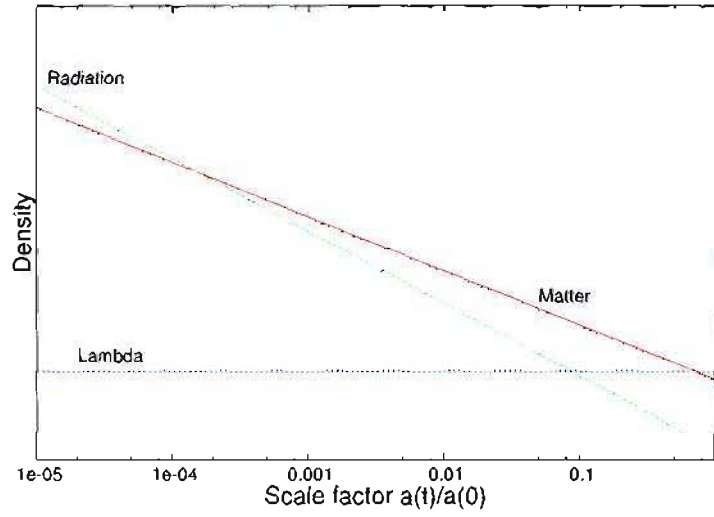 $$4\pi G \rho_m = \frac{3}{2}\Omega_m H^2 . \tag{B.29}$$

Figure B.2: Density versus Scale Factor

This shows the evolution of density with the scale factor. The density of radiation is depicted by the dotted line(blue), matter by the dashed line(green) and lambda by the solid line(red).

Substituting equation B.29 into equation B.25 gives

$$\ddot{\delta} + 2H\dot{\delta} - \frac{3}{2}\Omega_m(t)H^2\delta = 0 . \tag{B.30}$$

An expanding universe slows down the growth of fluctuations; instead of the exponential growth predicted by a static universe, we get a power law collapse. This is known as the *expansion civilising effect*.

B.4 Growth of Dark Matter Perturbations with Time

Assuming the 'concordance' model for the universe (see table 1.1) the history of the universe can be divided into three distinct eras, depending on the dominant component at the time.

$$
\begin{aligned}
&\text{Radiation} : \rho_r \propto t^{-4} \\
&\text{Matter} \quad : \rho_m \propto t^{-3} \\
&\Lambda \qquad \quad : \rho_\Lambda \propto \text{constant}.
\end{aligned}
\tag{B.31}
$$

Early on, the universe was radiation dominated, but ρ_r drops rapidly with time, allowing matter to become the dominant component. As time continues, matter density continues to decrease (at a rate slower than that of the radiation density) until a point where it drops below the cosmological constant density. This is shown in figure B.2. We will now discuss the evolution of matter fluctuations in each of these eras.

1. Radiation dominated Era

We first consider the growth of matter fluctuations in a radiation dominated era. In the radiation dominated era $H = \frac{\dot{a}}{a} = \frac{1}{2t}$.

$$
\Omega_m = \frac{\rho_m}{\rho_c} = \frac{\rho_m}{\rho_{total}} \frac{\rho_{total}}{\rho_c} \ll 1
$$
$$
\text{since } \frac{\rho_{total}}{\rho_c} = 1 \text{ and } \rho_m \ll \rho_{total}.
$$

and equation B.30 becomes

$$
\ddot{\delta} + \frac{1}{t}\dot{\delta} = 0 ,
\tag{B.32}
$$

which has the general solution

$$
\delta_m = B_1 + B_2 \ln t .
\tag{B.33}
$$

The growth of matter fluctuations in a radiation dominated era is logarithmic.

2. Λ dominated Era

In a Λ dominated model matter is subdominant ($\Omega_m \ll 1$).
$H_\Lambda = \frac{\dot{a}}{a} = \sqrt{\frac{\Lambda}{3}}$ since $a \propto e^{\left(\sqrt{\frac{\Lambda}{3}}t\right)}$. H_Λ is a constant.

Using this in equation B.30 we get

$$\ddot{\delta} = 2 H_\Lambda \dot{\delta} = 0 \tag{B.34}$$

which has the solutions

$$\delta_m = c_1 + c_2 e^{-2 H \Lambda t} . \tag{B.35}$$

This means that the matter density fluctuations in a Λ dominated era will reach a constant size while the average matter density falls as $\bar{\rho}_m \propto a^{-3} \propto e^{-3 H_\Lambda t}$. In this scenario, structure formation will stagnate.

3. The Matter dominated Era

Finally, we consider the case of a matter dominated era. During this era $a \propto t^{\frac{2}{3}}$ which makes $H = \frac{2}{3}t$. Also, $\Omega_m = \frac{\bar{\rho}_m}{\rho_c} = 1$.

This means that equation B.30 can be written as

$$\ddot{\delta} + \frac{4}{3}t\dot{\delta} - \frac{2}{3}t^2 = 0 \tag{B.36}$$

which has the solutions

$$\delta(t) \propto t^n \qquad n = -1, n = \tfrac{2}{3}.$$

We can write these solutions as $\delta(t) = D_1 t^{\frac{2}{3}} + D_2 t^{-1}$, where D_1, D_2 are the growing and decaying modes respectively. The decaying mode becomes insignificant rapidly, and we will focus on the growing mode. In the growing mode

$\delta \propto t^{\frac{2}{3}} \propto a(t)$, the density fluctuation will grow with the expansion of the universe.

In the Linear theory ($\delta \ll 1$) the overdensity will grow with the expansion of the universe. As the universe expands, δ grows. As δ becomes $\mathcal{O}(1)$ non-linear theory is required to understand the development. We do know that, at this stage, the overdensity will break away from the expansion and collapse under gravity.

The discussion above was for dark matter only, that is, for collisionless, dissipationless matter. Baryons are not dissipationless; they will radiate heat, cool and fall to the centre of the halo. The dark halo will extend far beyond the boundaries of the galaxy.

The discussion was also limited to linear theory where $\delta \ll 1$ clearly, a non-linear approach is needed to understand structure formation beyond this point. Galaxies and galaxy clusters have $\delta \sim 10^2 - 10^3$. To study this behaviour we will use a numerical approach. This is discussed in detail in chapter 2.

Appendix C

Rigid Body Rotation

In this project, we study the rotation of the dark matter halos produced in cold dark matter simulations, trying to determine whether or not there is any appreciable rotation of the halo as a whole. Here we discuss rigid body rotation in general, following the approach taken by Goldstein [1980].

A rigid body can be defined as a collection of particles whose relative distances remain fixed. Of course, this is only an idealised model as the constituent particles within the parent body will usually be free to move, and will undergo some relative motion. Fortunately, the scale of this motion is usually microscopic in relation to the rotation of the body and the relative motion of the particles can usually be safely ignored. Also, in real systems, forces on the system will cause it to deform, affecting the shape of the body. This effect will be neglected in the following discussion; we will assume our rigid body to have a definite, unchanging shape.

In order to fully specify the position of a body, only six co-ordinates are needed. These are often taken to be the co-ordinates of the body's centre of mass, and three independent angles, which will give the orientation of the body co-ordinate system with respect to the fixed (or inertial) system. In order to simplify the problem, the center of mass can often be made to coincide with the origin of the body co-ordinate system.

Any finite motion of a rigid body can be regarded as the sum of two independent motions - a linear translation of some point, and the rotation of the body about that point.

Consider a rigid body, composed of N particles with masses m_α where $\alpha = 1, 2 \ldots N$. Let the body rotate with an instantaneous angular velocity ω about a point fixed with respect to the body co-ordinate system. And let the body move with an instantaneous velocity V with respect to the fixed co-ordinate system. Then the instantaneous velocity of a particle in the fixed system can be expressed as:

$$\mathbf{v}_f = \mathbf{V} + \mathbf{v}_r + \omega \times \mathbf{r} \tag{C.1}$$

where

$\mathbf{v}_f$ = velocity relative to the fixed axes.

$\mathbf{V}$ = linear velocity of the moving origin.

$\mathbf{v}_r$ = velocity relative to the rotating axes.

ω = angular velocity of the rotating axes.

$\omega \times \mathbf{r}$ = velocity due to the rotation of the moving axes.

Since the body is rigid all velocities with respect to the rotating or body system are zero ($\mathbf{v}_r = 0$). The remaining velocities are understood to be with respect to the fixed system.

C.1   Kinetic Energy of the Rigid Body

The kinetic energy of the αth particle is given by:

$$T_\alpha = \frac{1}{2} m_\alpha v_\alpha^2 . \tag{C.2}$$

The total kinetic energy is then given by the sum of T_α over all particles, replacing v_α with equation C.1.

$$T = \frac{1}{2} \sum_\alpha m_\alpha V^2 + V \cdot \boldsymbol{\omega} \times \sum_\alpha m_\alpha \mathbf{r}_\alpha + \frac{1}{2} \sum_\alpha m_\alpha \left(\boldsymbol{\omega} \times \mathbf{r}_\alpha \right)^2 . \tag{C.3}$$

Equation C.3 is a general expression for the kinetic energy of a system and is valid for any choice of origin. However, it is often convenient to chose the origin to coincide with the center of mass of the body, making the second term in equation C.3 zero. Following this choice of origin, the kinetic energy can then easily be expressed as the sum of two independent parts:

$$T = T_{translation} + T_{rotation}$$

where

$$T_{\text{translation}} = \tfrac{1}{2} \sum_\alpha m_\alpha V^2$$
$$T_{\text{rotation}} = \tfrac{1}{2} \sum_\alpha m_\alpha \left(\boldsymbol{\omega} \times \mathbf{r}_\alpha \right)^2 .$$

The kinetic energy has been separated into a component due to translation and a component due to rotation.

Consider the rotational kinetic energy. Using the identity

$$(\mathbf{A} \times \mathbf{B})^2 = (\mathbf{A} \times \mathbf{B}) \cdot (\mathbf{A} \times \mathbf{B}) = A^2 B^2 - (\mathbf{A} \cdot \mathbf{B})^2 \tag{C.4}$$

and expressing $\mathbf{r}_\alpha = (x_{\alpha,1}, x_{\alpha,2}, x_{\alpha,3})$ the rotational kinetic energy can be re-written as:

$$T_{\text{rotation}} = \frac{1}{2} \sum_{i,j} \omega_i, \omega_j \sum_\alpha m_\alpha \left[\delta_{ij} \sum_k x_{\alpha,k}^2 - x_{\alpha,i} x_{\alpha,j} \right] . \tag{C.5}$$

If we define the ij^{th} element of the sum over α to be I_{ij} such that:

$$I_{ij} = \sum_{\alpha} m_{\alpha} \left[\delta_{ij} \sum_{k} x_{\alpha,k}^2 - x_{\alpha,i} x_{\alpha,j} \right] , \qquad (C.6)$$

then we have

$$T_{\text{rotation}} = \frac{1}{2} \sum_{i,j} I_{i,j} \omega_i \omega_j . \qquad (C.7)$$

I_{ij}, as defined in equation C.6, is known as the Inertia Tensor.

C.2 Angular Momentum of the Rigid Body

Using a similar approach, we now consider the angular momentum of a system. The angular momentum of a body with respect to some fixed point (O) in the body co-ordinate system is given by:

$$\mathbf{L} = \sum_{\alpha} \mathbf{r}_{\alpha} \times \mathbf{p}_{\alpha} . \qquad (C.8)$$

The momentum of the αth particle is $\mathbf{p}_{\alpha} = m_{\alpha} \mathbf{v}_{\alpha} = m_{\alpha} (\boldsymbol{\omega} \times \mathbf{r}_{\alpha})$. Using this, and the identity given by equation C.4, we can rewrite equation C.8 as follows

$$\mathbf{L} = \sum_{\alpha} m_{\alpha} \left[\mathbf{r}_{\alpha}^2 \boldsymbol{\omega} - \mathbf{r}_{\alpha} \left(\mathbf{r}_{\alpha} \cdot \boldsymbol{\omega} \right) \right] . \qquad (C.9)$$

If we now consider the angular momentum in terms of the components of $\boldsymbol{\omega}$ and $\mathbf{r}_{\alpha}$, using $\mathbf{r}_{\alpha,i} = x_{\alpha,i}$ we can write the ith component of the angular momentum as:

$$L_i = \sum_{\alpha} m_{\alpha} \left[\omega_i \sum_{k} x_{\alpha,k}^2 - x_{\alpha,i} \sum_{j} (x_{\alpha,j} \omega_j) \right] \qquad (C.10)$$

90

or

$$L_i = \sum_j \omega_j \sum_\alpha \left[\delta_{ij} \sum_k x_{\alpha,k}^2 - x_{\alpha,i} x_{\alpha,j} \right] \tag{C.11}$$

if we use $\omega_i = \sum_j \omega_i \delta_{ij}$. Using definition of I_{ij} (equation C.6) we see that the angular momentum can be expressed as

$$L_i = \sum_j I_{ij} \omega_j \,. \tag{C.12}$$

Appendix D

Pattern Speed Fits

This appendix gives additional pattern speed fits, for all halos identified as undergoing coherent rotation. Figure D.1 shows the pattern speed fits obtained for all of the halos found to be undergoing coherent rotation over both one and three gigayear periods, over a period of one gigayear. The first 25 plots are the fits to halos exhibiting pattern speeds larger than 3 times the estimated error. The last 5 show detections above twice the error but below three times this value. Figure D.2 shows the fits to halos only identified as rotating over a one gigayear period. The first 11 plots show rotation speeds above three times the error.

Adjusting our cutoff so as to include only those halos with pattern speeds above three times the error does not significantly change the pattern speed distribution, best fit values for this selection were $\mu = -0.88$ and $\sigma = 0.34$.

Figure D.3 shows the pattern speed fits obtained for all of the halos found to be undergoing coherent rotation over both one and three gigayear periods, over a period of three gigayears. The first 26 plots show halos with measured pattern speeds greater than 3 times the error. The last 4 show detections above twice the error but below 3 times this value. As we found with our one gigayear sample, adjusting our cutoff to include only those halos with pattern speed detections greater than 3 times the error

does not significantly change the pattern speed distribution, best fit values for this selection were $\mu = -1.03$ and $\sigma = 0.31$.
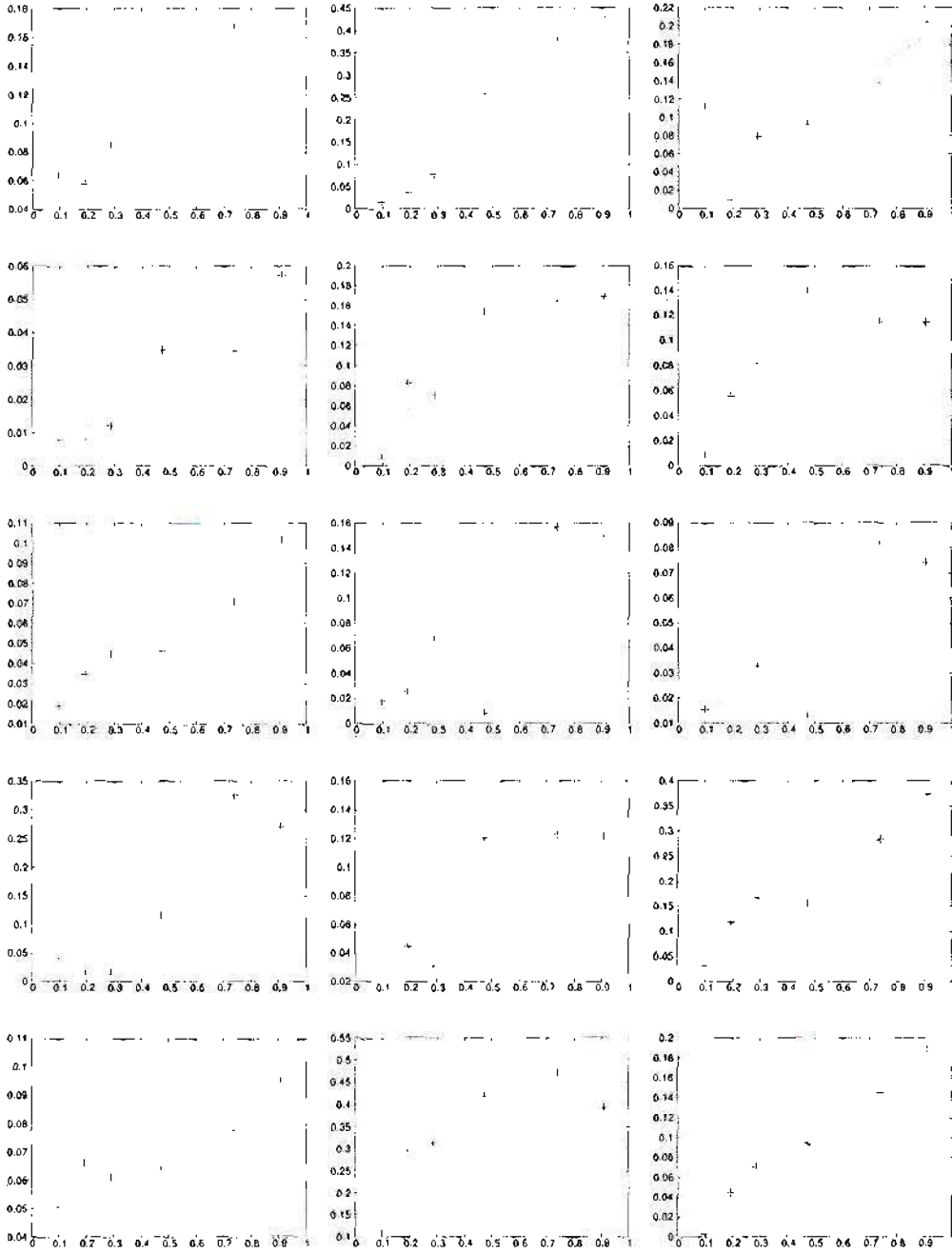
Figure D.1: Pattern Speed Fits: Coherent Rotation over 1 & 3 Gyrs (1 Gyr fit).
This figure shows the pattern speed fits to all of the halos identified as rotating over both one and three gigayear periods, over the one gigayear period. The horizontal axis gives the time in h^{-1} gigayears and the vertical axis gives the rotation in radians. The first 25 plots show the fits to halos exhibiting pattern speeds greater than 3 times the estimated error.
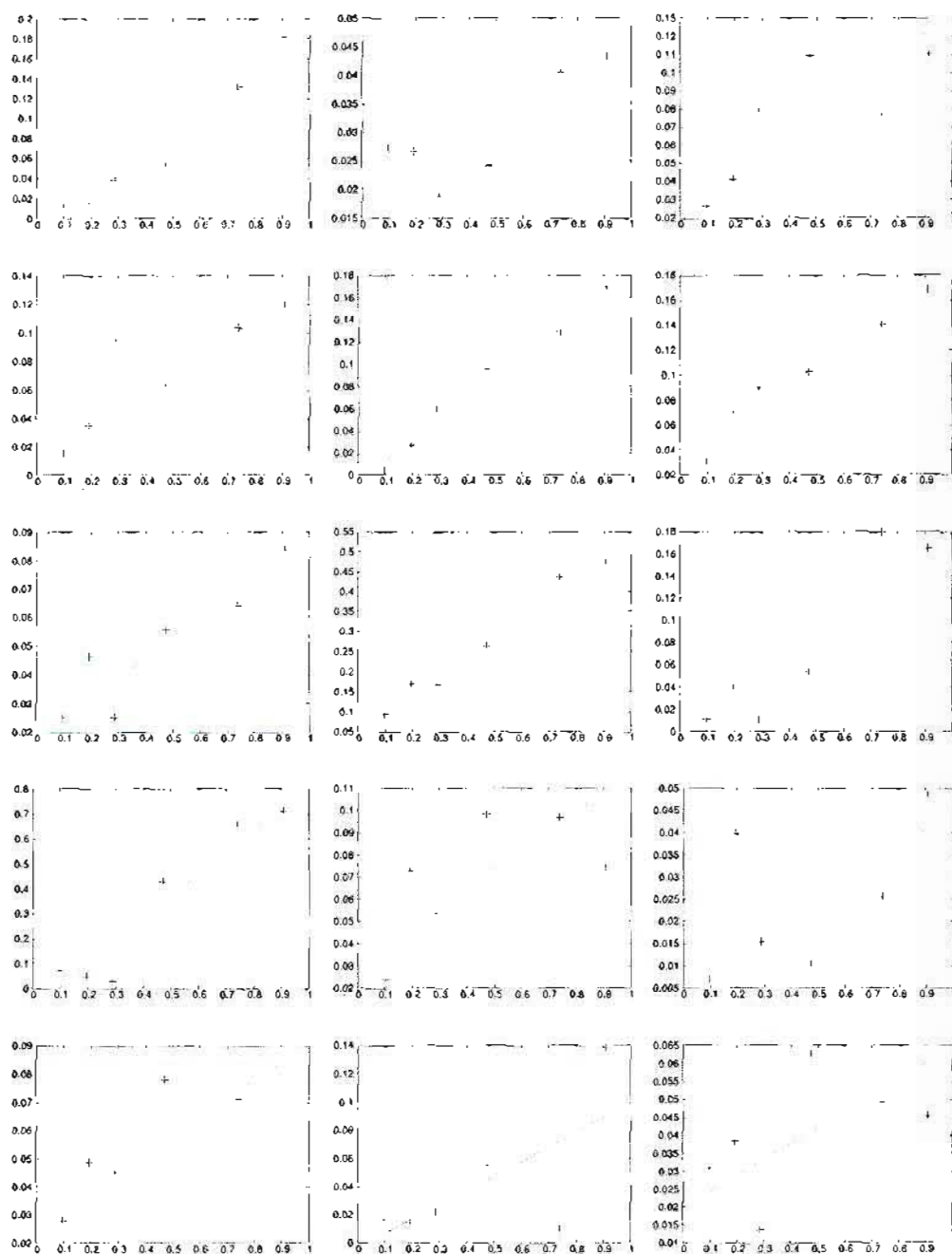
Figure D.1 continued.

95
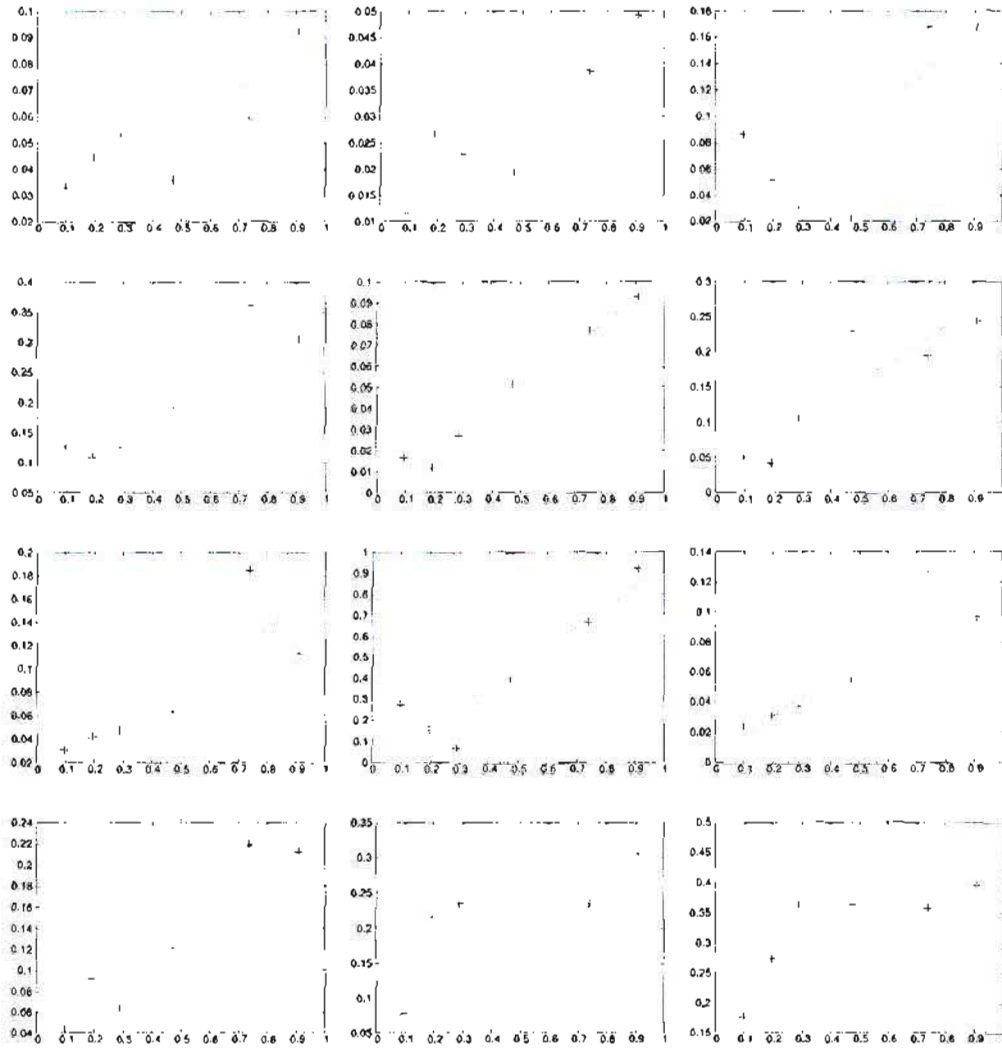
Figure D.2: Halos Identified as Rotating over One Gigayear Only.
The horizontal axis gives the time in h^{-1} gigayears and the vertical axis gives the rotation in radians.
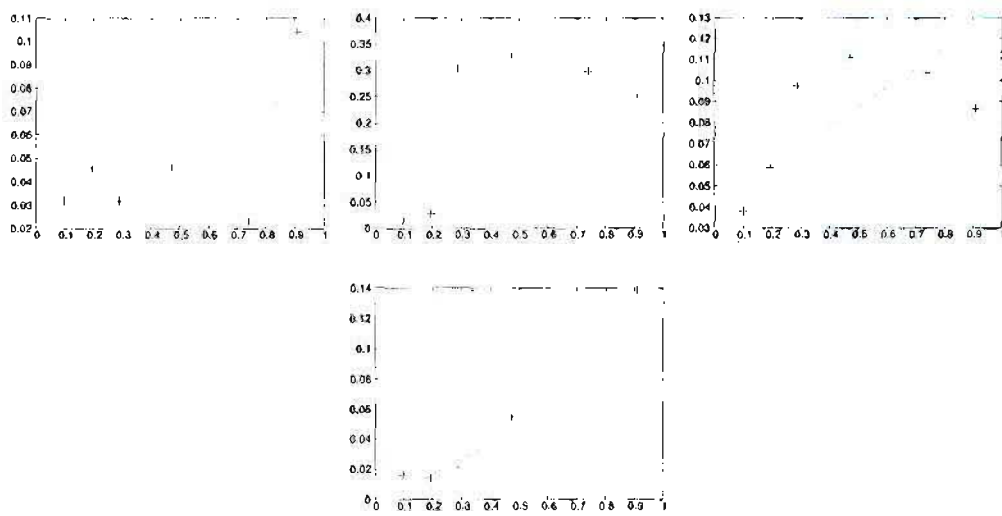The first 11 plots show pattern speeds greater than three times the estimated error.
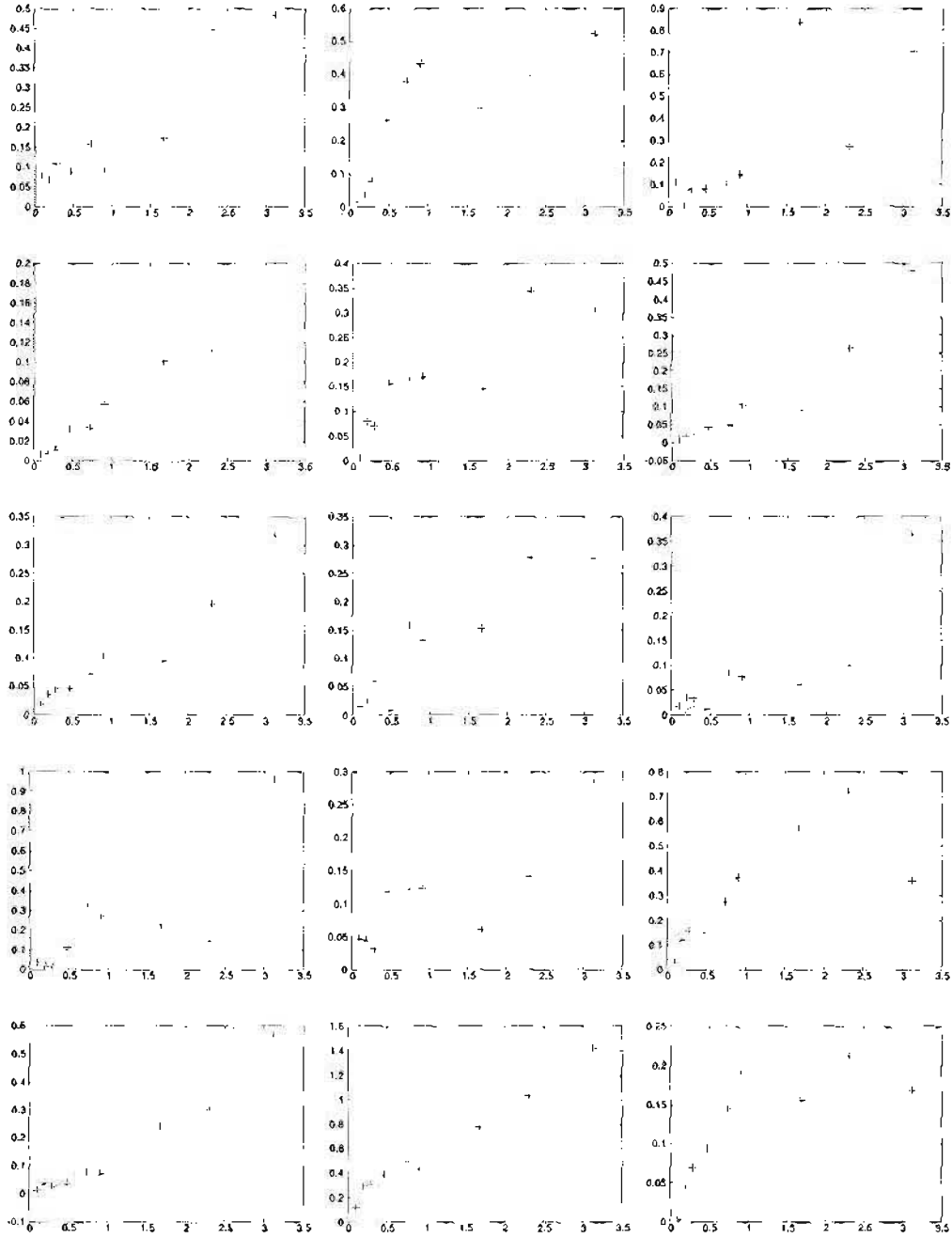
Figure D.2 continued.

Figure D.3: Pattern Speed Fits: Coherent Rotation over 1 & 3 Gyrs (3 Gyr fit).
This figure shows the pattern speed fits to all halos identified as rotating over both one and three gigayear periods. The horizontal axis gives the time in h^{-1} gigayears and the vertical axis gives the rotation in radians. The first 26 plots depict pattern speeds greater than three times the estimated error.
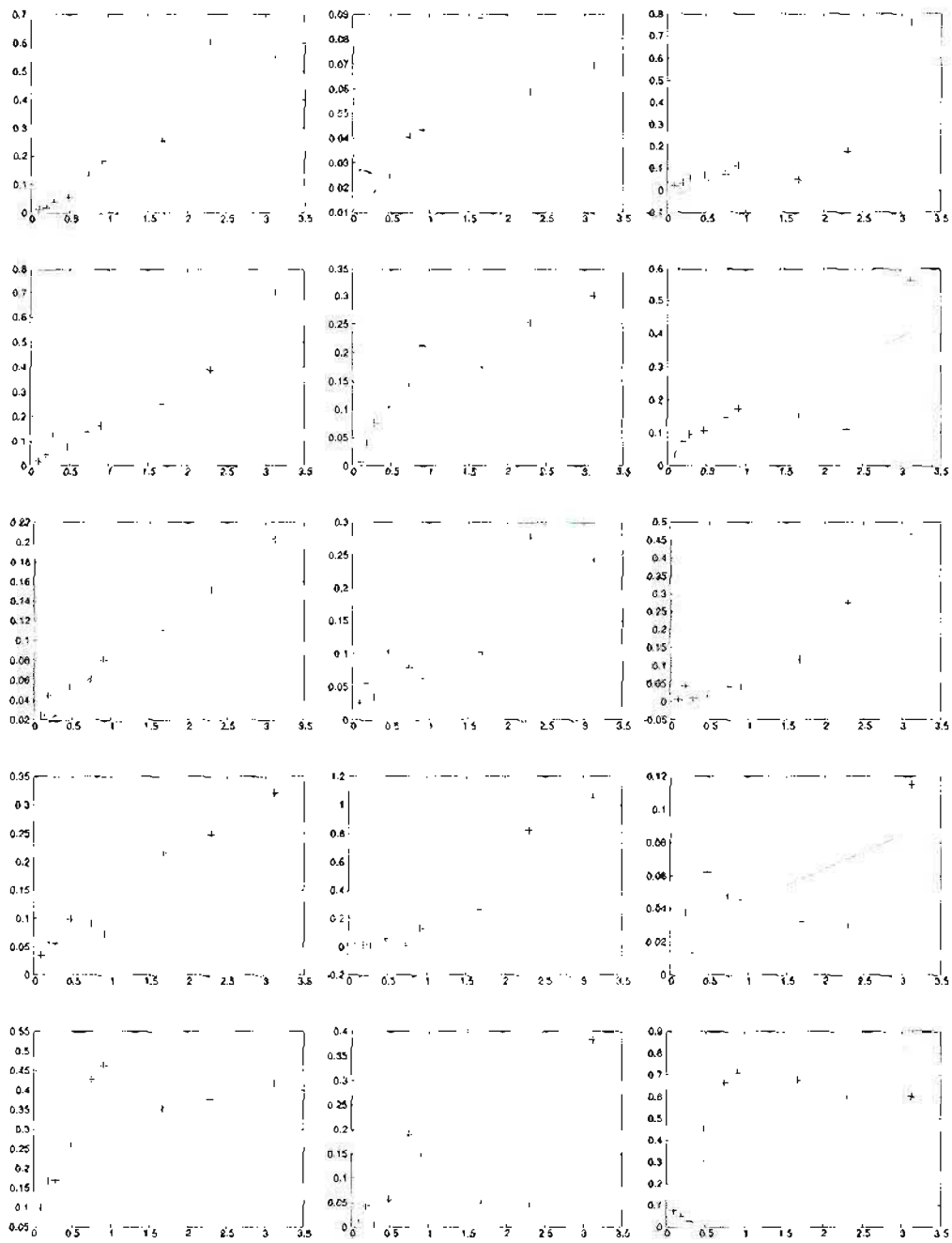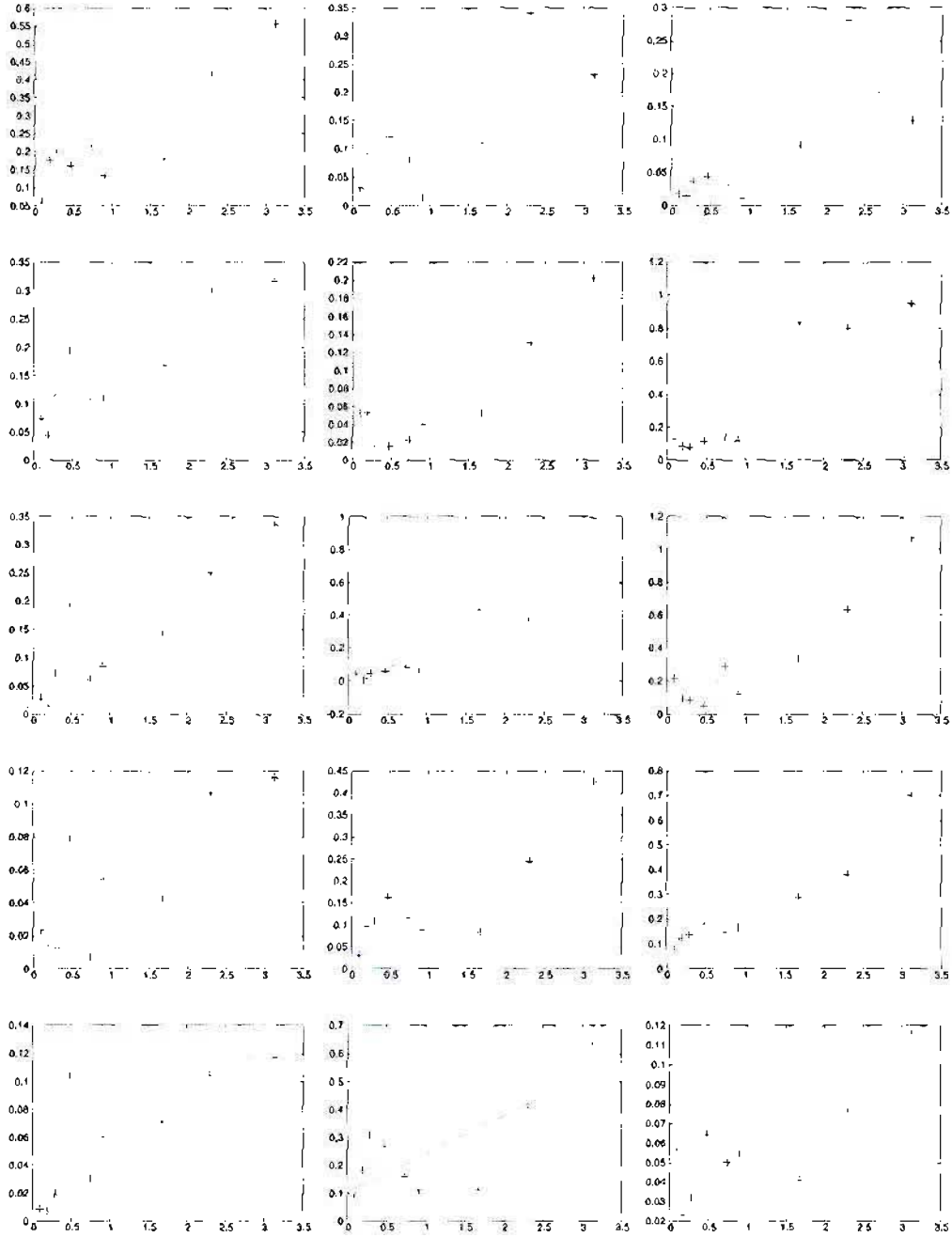
98

Figure D.3 continued.

Figure D.4: Halos Identified as Rotating over 3 Gigayears Only.
The horizontal axis gives the time in h^{-1} gigayears and the vertical axis gives the rotation in radians. The first 17 plots show pattern speeds greater than three times the estimated error.
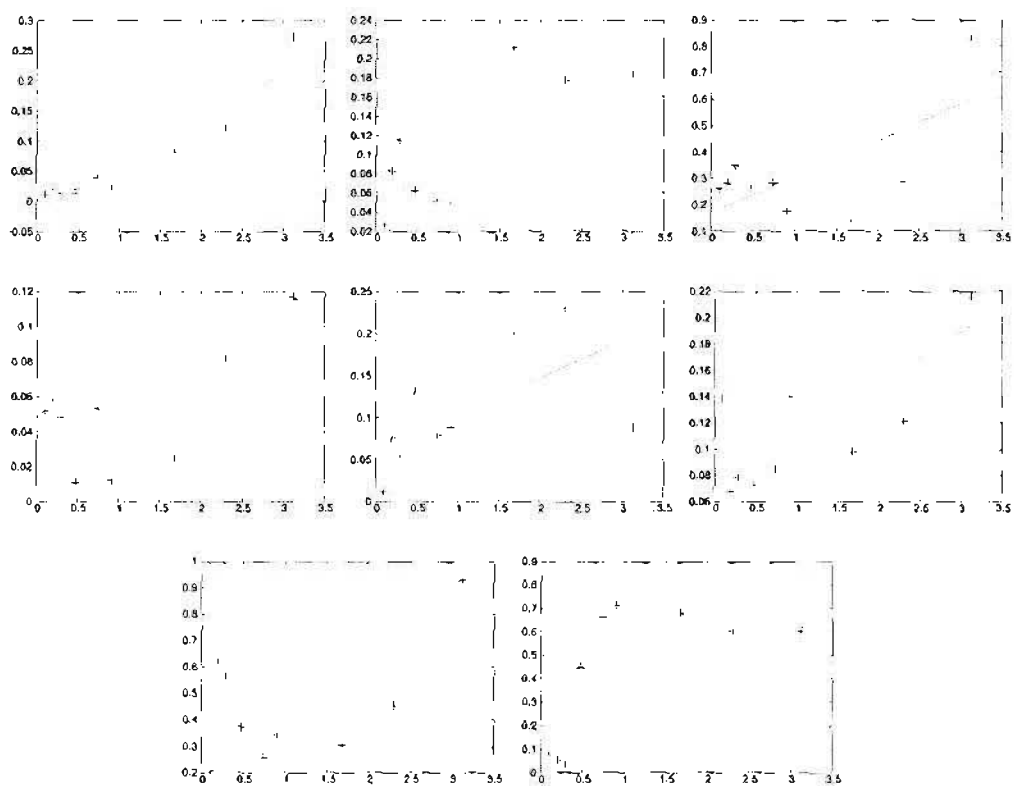
Figure D.4 continued.